

ARTICLE TEMPLATE

Decadal analysis of sea surface temperature patterns, climatology, and anomalies in temperate coastal waters with Landsat-8 TIRS observations

Yiqing Guo^a, Nagur Cherukuru^b, Eric Lehmann^a, Xiubin Qi^c, Mark Doubell^d,
S. L. Kesav Unnithan^b, Ming Feng^e

^aCSIRO Data61, Acton, ACT 2601, Australia;

^bCSIRO Environment, Acton, ACT 2601, Australia;

^cCSIRO Space and Astronomy, Kensington, WA 6151, Australia;

^dSouth Australian Research and Development Institute, West Beach, SA 5024, Australia;

^eCSIRO Environment, Crawley, WA 6009, Australia

ARTICLE HISTORY

Compiled March 11, 2025

ABSTRACT

Sea surface temperature (SST) is a fundamental physical parameter characterising the thermal state of sea surface. Due to the intricate thermal interactions between land, sea, and atmosphere, the spatial gradients of SST in coastal waters often appear at finer spatial scales than those in open ocean waters. The Thermal Infrared Sensor (TIRS) onboard Landsat-8, with its 100-meter spatial resolution, offers a unique opportunity to uncover fine-scale coastal SST patterns that would otherwise be overlooked by coarser-resolution thermal sensors. In this study, we first develop an operational approach for SST retrieval from the TIRS sensor, and subsequently propose a novel algorithm for establishing daily SST climatology which serves as the baseline to detect anomalous SST events. We applied the proposed methods to temperate coastal waters in South Australia for the ten-year period from 2014 to 2023. For ground validation purposes, a buoy was deployed off the coast of Port Lincoln, South Australia, to record in-situ time-series SST. The spatiotemporal patterns of SST in the study area were analysed based on the ten years of satellite-derived SST imagery. The daily baseline climatology of SST with 100 m resolution

was constructed, which allowed for the detection and analysis of anomalous SST events during the study period of 2014–2023. Our results suggest the following: (1) the satellite-derived SST data, generated with the proposed algorithm, aligned well with the in-situ measured SST values; (2) the semi-enclosed, shallow regions of Upper Spencer Gulf and Upper St Vincent Gulf showed higher temperatures during summer and cooler temperatures during winter than waters closer to the open ocean, resulting in a higher seasonal variation in SST; (3) the near-shore shallow areas in Spencer Gulf and St Vincent Gulf, and regions surrounding Kangaroo Island, were identified to have a higher probability of SST anomalies compared to the rest of the study area; and (4) anomalous SST events were more likely to happen during the warm months (January–March and October–December) than the cool months (April–September). These findings may offer valuable guidance to inform the local fishing and aquaculture industries in optimising their practices. The SST product and baseline SST climatology derived in this study have been made available for public access (please refer to the Data Availability section for details).

KEYWORDS

Sea surface temperature; Landsat-8 TIRS; coastal waters; radiative transfer; thermal infrared; spatiotemporal analysis; baseline climatology; anomaly detection

1. Introduction

Sea surface temperature (SST) is an important geophysical variable, because it not only characterises the thermal state of sea surface but also influences the health of marine ecosystems [1–3]. Quantitative retrieval of SST from spaceborne measurements has been one of the primary objectives for many Earth observation missions since the 1970’s [4–6]. Considering that satellite remote sensing is a powerful tool for rapid and large-scale mapping and monitoring (*e.g.*, [7–9]), SST maps derived from spaceborne thermal infrared instruments provide critical observational evidence to a wide range of environmental applications, including deriving water temperature climatology and detecting anomalous temperature events (*e.g.*, [10–13]).

High-quality SST retrieval from top-of-atmosphere thermal infrared measurements requires accurate correction of atmospheric effects [1, 14]. Water-emitted thermal radiance at sea level differs from that measured by spaceborne sensors due to the interference of atmosphere in the following two respects. Firstly, the thermal radiance emitted from

water is scattered and absorbed by constituents of atmosphere, resulting in an attenuated signal to be captured by the sensor. Secondly, the atmosphere also emits thermal radiance by itself, superimposing water-emitted radiance. Such atmospheric interference should be appropriately corrected, in order to recover the thermal signals radiated by sea water. Considering that the circumstance of atmosphere shifts from time to time and from location to location, it would be preferred to utilise specific atmospheric conditions at the time and location of each satellite image acquisition, rather than those sampled from a standard atmosphere database, to ensure the quality of atmospheric correction.

Although Landsat satellites are primarily designed for observing Earth’s land-masses, the image footprints are able to cover sea waters close to coastline, making them suitable for coastal water monitoring. In particular, the Thermal Infrared Sensor (TIRS) onboard NASA/USGS Landsat-8 has been deemed as adequate for quality retrieval of SST [14–18]. The instrument measures thermal radiance at two separate spectral channels, *i.e.*, 10.60–11.19 μm (Band 10) and 11.50–12.51 μm (Band 11) [19]. Previous studies have reported that single-channel algorithms [20, 21] based on rigorous radiative transfer modelling demonstrated adequate accuracy in surface temperature retrieval over both land [22] and water [14]. The TIRS has a spatial resolution of 100 m [19], finer than the thermal bands of earlier Landsat satellites and several other spaceborne instruments like MODIS (1 km) [23], VIIRS (750 m) [24], and Sentinel-3 SLSTR (1 km) [25]. Given that the spatial gradients of SST in coastal waters often present at smaller spatial scales than those in open ocean waters, high-resolution SST data such as those derived from TIRS may help enhance our understanding of coastal SST patterns.

The temperate coastal waters of South Australia, including Spencer Gulf, St Vincent Gulf, and their adjacent waters, are ecologically significant and economically vital [26]. This region supports several local industries, including fishing and aquaculture, and is home to a range of marine species, such as the endangered Great White Shark [27]. Informed decision-making for local communities and industries depends on high-quality SST climatology data specific to South Australia’s coastal waters. The SSTAARS (Sea Surface Temperature Atlas of the Australian Regional Seas) dataset [28] has been a reliable source of baseline SST climatology, supporting studies on marine heatwave de-

tection (*e.g.*, [29, 30]) and ocean current analysis (*e.g.*, [31, 32]). However, its spatial resolution, at a relatively coarse 2 km, may limit its applicability in studies requiring finer-scale oceanographic details. In particular, the complex meandering coastline and small-scale SST features in South Australia’s coastal waters necessitate a finer spatial resolution for SST climatology to capture the localised thermal dynamics. The 100 m resolution TIRS observations thus present an opportunity to extract SST climatology with enhanced spatial detail compared to state-of-the-art climatology products such as SSTAARS.

Anomalous SST events that deviate from the baseline climatology impact fishery and aquaculture practices, as well as the health of marine ecosystems. South Australia’s coastal waters are influenced by the interaction of large-scale ocean currents, such as the warm Leeuwin Current Extension flowing from the Indian Ocean along the southern coastline [33] and the cooler Flinders Current originating from the Southern Ocean [34]. The two large triangular-shaped gulfs, namely the Spencer Gulf and St Vincent Gulf, enclose waters characterised by regional circulation. These geographical factors, along with land-water interactions and vertical upwelling dynamics, contribute to the high frequency of SST anomalies in South Australia’s coastal waters, as reported in [35, 36]. To assist local communities and industries in mitigating the potential adverse effects of anomalous SST events, a clearer understanding of their spatiotemporal distribution is essential.

In this study, we aim to analyse the SST patterns, climatology, and anomalies in temperate coastal waters off the South Australian coast with high-resolution satellite observations for the ten-year period from 2014 to 2023. We first develop an operational approach for SST retrieval from the Landsat-8 TIRS sensor, followed by proposing a novel algorithm for establishing daily SST climatology which serves as the baseline for detecting anomalous SST events. Specifically, this work aims to achieve the following objectives.

- (1) We develop an operational approach for high-quality SST retrieval from the Landsat-8 TIRS sensor, with rigorous radiative transfer modelling and spatiotemporally specific atmospheric data being applied for correcting atmospheric effects;

- (2) We propose a novel algorithm to establish the daily baseline SST climatology at a spatial resolution of 100 m, which is finer than state-of-the-art climatology datasets such as the 2 km resolution SSTAARS [28];
- (3) We compile the probability map of anomalous SST events in the study area with SST images over 2014–2023, and analyse the spatial and seasonal distribution of these anomalies; and
- (4) We introduce a tile-based parallelisation scheme for efficient processing across large spatial scales, with the derived SST product and baseline SST climatology for the study area being made available for public access (please refer to the Data Availability section for details on data access).

The rest of the paper is organised as follows. Section 2 introduces the study area and the datasets used for modelling and validation. Section 3 describes the methodologies for SST retrieval and spatiotemporal analysis. Section 4 presents the validation and analysis results, and discusses the findings and limitations of this work. Finally, Section 5 concludes the paper.

2. Study Area and Data Sets

2.1. Study Area

This work was focused on Australian territorial waters off the coast of South Australia (134°30'00"–140°00'00"E, 32°25'58"–36°30'00"S), including Spencer Gulf, St Vincent Gulf, and their adjacent waters, as shown in Figure 1. The shape files defining the coastline and territorial water limit are available from the Australian Bureau of Statistics [37]. Major townships surrounding these waters include Adelaide (the capital city of South Australia, located on the east bank of St Vincent Gulf), Port Lincoln (located on the west bank of Spencer Gulf), and Port Augusta (situated at the north end of Spencer Gulf) (Figure 1). The Kangaroo Island is located to the south of Spencer Gulf and St Vincent Gulf (Figure 1). This temperate coastal region has a Mediterranean climate, with hot and dry summers, and mild and wet winters. Air temperatures range from 18.5°C to 29.2°C in January, and from 7.2°C to 16.9°C in July. The area receives

moderate rainfall, averaging 277.5 mm per year, with most of it falling during the winter months, according to statistics from Australian Bureau of Meteorology¹.

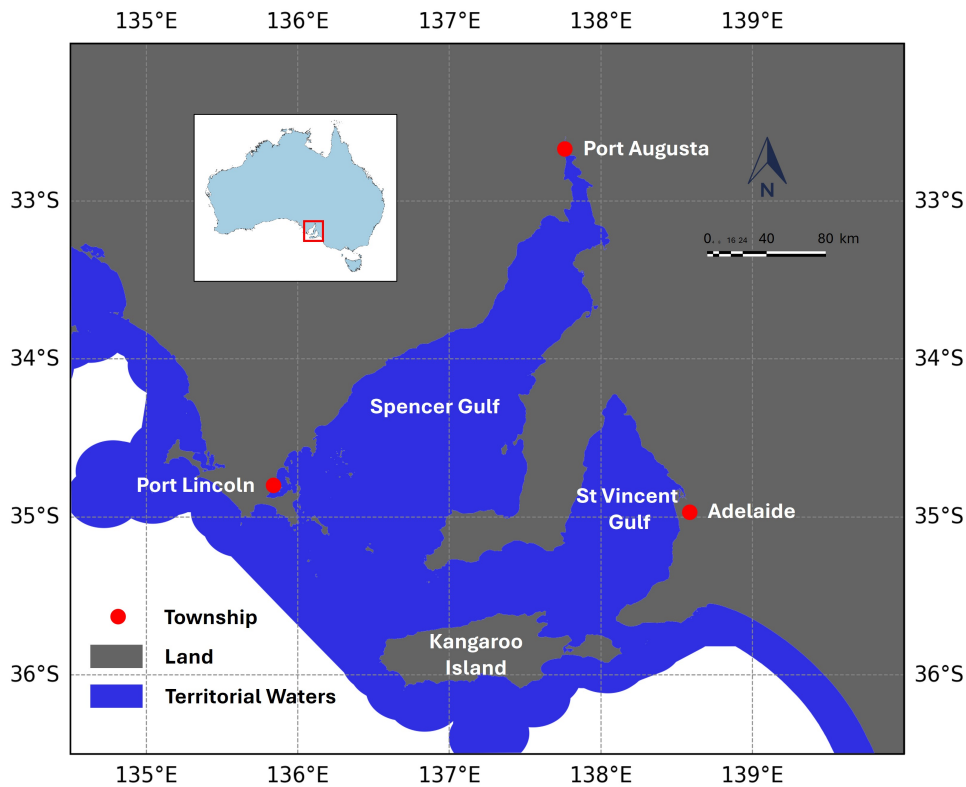


Figure 1. The study area of this work encompasses the Australian territorial waters off the coast of South Australia, including Spencer Gulf, St Vincent Gulf, and their adjacent waters.

2.2. Satellite Imagery

As the thermal infrared instrument onboard NASA/USGS Landsat-8 satellite, TIRS is capable of measuring thermal radiation emitted from Earth's surface. It records thermal radiance at two separate spectral channels, *i.e.*, 10.60–11.19 μm (Band 10) and 11.50–12.51 μm (Band 11), with a spatial resolution of 100 m. The TIRS has a swath width of 185 kilometres, aligning with the coverage of Operational Land Imager (OLI) onboard the same satellite. In this study, the Landsat-8 Collection 2 Level-1C TIRS product was used. It consists of top-of-atmosphere thermal infrared data with radiometrical calibration and geometrical correction having been applied. TIRS images covering the study area from 2014 to 2023 were queried within the AquaWatch Data Service (ADS)

¹http://www.bom.gov.au/climate/averages/tables/cw_018103.shtml

built upon CSIRO’s Earth Analytics and Science Innovation (EASI) platform. An Open Data Cube (ODC) environment [38, 39] was set up on the platform to facilitate data processing. The total number of satellite observations from 2014 to 2023 varies across the study area, ranging from 127 to 431 records, as shown in Figure 2a. Regions with overlapping satellite scenes show a higher observation frequency. Cloud cover is frequent in the study region, as shown in Figure 2b, with the percentage of cloudy observations ranging from 30.6% to 72.9%. The lowest cloud percentage is observed in the Upper Spencer Gulf, and the highest over the ocean south of Kangaroo Island. In this study, pixels flagged as cloud or cirrus by the Landsat Collection 2 Pixel Quality Assessment Band were masked out from our processing. In addition to these Landsat-8 TIRS images, we also queried Landsat-8 OLI Level-2 surface reflectance images and MODIS Terra Level-2 SST images for quality control and intercomparison purposes.

2.3. Coincident Atmosphere Data

The atmosphere data spatiotemporally coincident with each satellite observation were retrieved from the CAMS global reanalysis (EAC4) dataset [40], provided by the Copernicus Atmosphere Monitoring Service (CAMS) at the European Centre for Medium-Range Weather Forecasts (ECMWF). We chose to use spatiotemporally specific atmosphere data at the time and location of each satellite observation, rather than the data of a standard atmosphere, aiming to improve the modelling accuracy of SST retrievals. The EAC4 dataset provides high-quality atmosphere data at a 3-hour temporal interval and a spatial resolution of approximately 80 km. These data were queried using the Climate Data Store Application Program Interface (CDSAPI) from the Atmosphere Data Store, where the data were provided in an interpolated $0.75^\circ \times 0.75^\circ$ lon/lat grid. The vertical profiles of air pressure (in unit of Pa; Figure 3a), air temperature (in K; Figure 3b), specific humidity (in kg/kg; Figure 3c), ozone content (in kg/kg; Figure 3d), and nitrogen dioxide content (in kg/kg; Figure 3e) were retrieved. These profiles were provided at 60 vertical levels of the standard atmosphere model as defined by the United States Standard Atmosphere, 1976 [41]. It is worth noting that the model levels are associated with air pressure rather than elevation. We therefore interpreted these model levels according to [42], and converted them into altitudes (in km relative to the sea

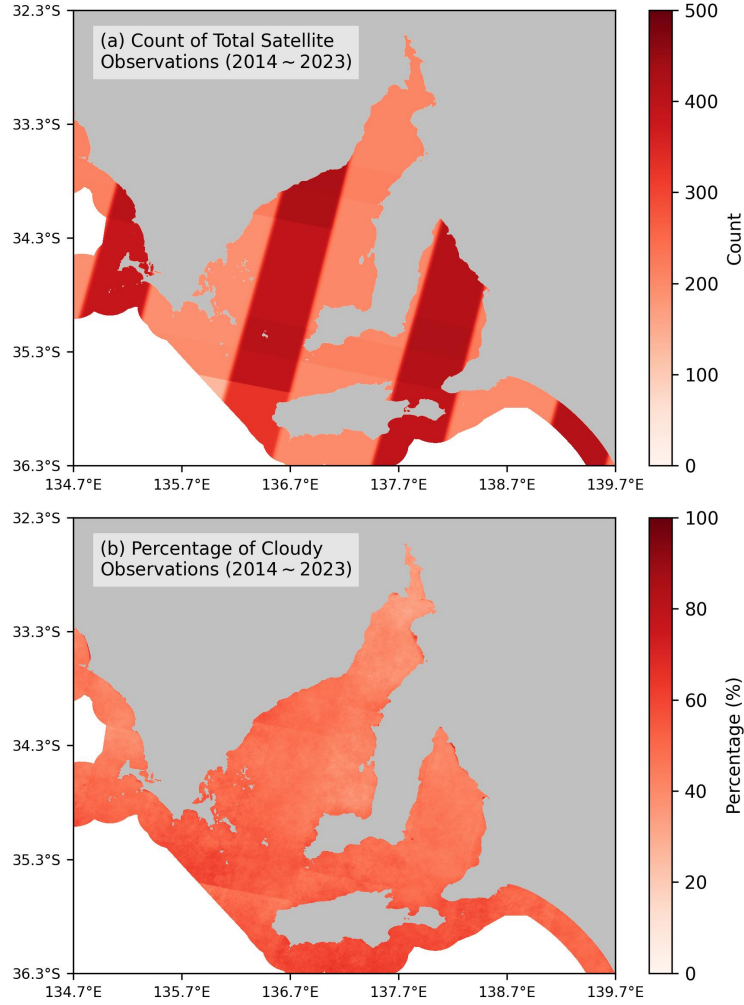


Figure 2. (a) The number of total satellite observations in the study area over 2014–2023, and (b) the chance of cloudy observations over the same time period as derived from the Landsat Collection 2 Pixel Quality Assessment Band.

level). The vertical profiles of non-trace gasses, including nitrogen, oxygen, and carbon dioxide contents (all in kg/kg; Figures 3f–h), were calculated based on their percentage constitutions in dry air moderated by the vertical distribution of specific humidity. The vertical profiles of water vapour pressure and dry air pressure (both in Pa; Figures 3i–j) were derived from air pressure and specific humidity based on the physical equations documented in [43, 44]. The vertical profile of air density (in kg/m³; Figure 3k) was then derived from dry air pressure and water vapour pressure based on the Ideal Gas Law. Finally, the vertical profile of water vapour content (in kg/m³; Figure 3l) was converted from air density and specific humidity. The detailed procedure of deriving these atmospheric profiles is described later in Subsection 3.4. These atmosphere data were

applied to SST modelling in this study.

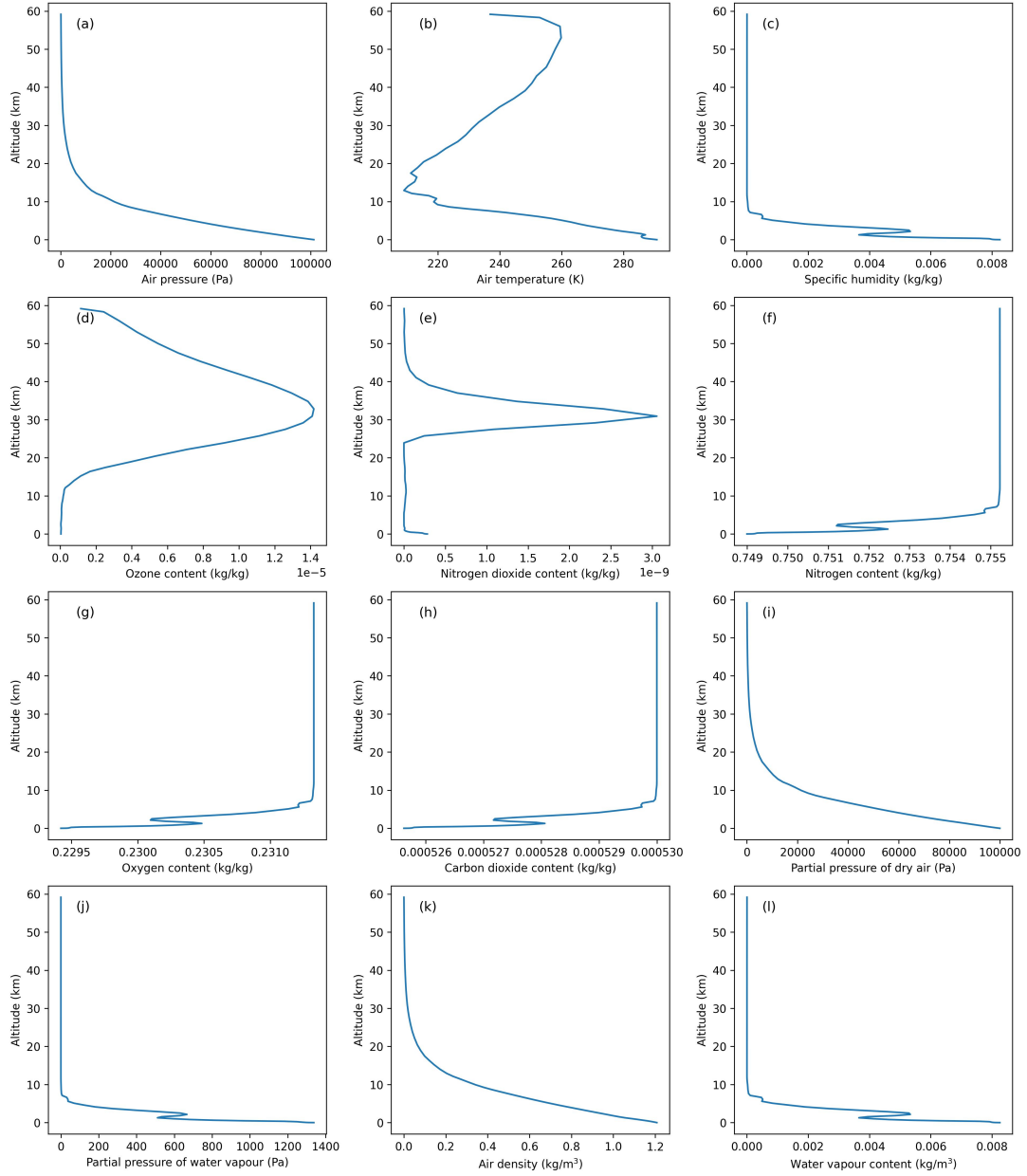


Figure 3. Example vertical profiles of (a) air pressure, (b) air temperature, (c) specific humidity, (d) ozone content, (e) nitrogen dioxide content, (f) nitrogen content, (g) oxygen content, (h) carbon dioxide content, (i) partial pressure of dry air, (j) partial pressure of water vapour, (k) air density, and (l) water vapour content from the sea surface (0 km altitude) to the top of atmosphere (60 km altitude).

2.4. Ground Truth Measurements

To validate the satellite-derived SST data in this study, we deployed a buoy off the coast of Port Lincoln, South Australia (135°54'01"E, 34°43'03"S), with support from

Table 1. List of offshore wave data buoys with their locations and record periods.

Station Name	Station Code	Location	Record Period
Batemans Bay Offshore Buoy	WAVEBAB	150°20'13"E, 35°42'28"S	01 Apr 2013 – 31 Dec 2015
Coffs Harbour Offshore Buoy	WAVECOH	153°15'32"E, 30°22'22"S	01 Apr 2013 – 31 Dec 2017
Crowdy Head Offshore Buoy	WAVECRH	152°51'08"E, 31°49'26"S	01 Apr 2013 – 31 Dec 2017

CSIRO’s AquaWatch Mission, as shown in Figure 4. A YSI EXO2 multiparameter sonde is mounted onto the buoy which streams in-situ temperature measurements every 10 min at a nominal depth of 1 m. The in-situ sensor has been in operation since 31 August 2022, with regular services and calibrations being conducted to ensure the quality of the data. These in-situ temperature measurements served as a reference for validating the satellite-derived SST data. For each satellite observation, the derived SST pixels covering a buffer zone of 3 km radius (excluding land pixels and near-shore pixels within 300 m to the coastline; Figure 4b), centred at the buoy location, were averaged and compared to the in-situ temperature reading closest to the acquisition time of satellite imagery. This averaging process aimed to increase the quantity of data points and provide a more robust SST estimate.

As an extended experiment to evaluate the performance of the proposed SST retrieval algorithm for temperate coastal waters beyond the study area, we sourced in-situ SST measurements from three buoys off the southeast coast of Australia [45]. These buoys, managed by the Manly Hydraulics Laboratory, provide high-quality SST records in New South Wales coastal waters. The SST records were collected using a thermistor located at the base of the buoy approximately 0.5 meters below the water surface [45]. Table 1 details the station name, station code, location, and record period for each buoy.

3. Methods

3.1. Overview

In this study, we aim at analysing the spatiotemporal dynamics of SST in temperate coastal waters in South Australia with satellite-derived SST measurements. We first develop an operational approach to retrieving SST from Landsat-8 TIRS observations over large spatiotemporal scales, followed by introducing statistical analyses to examine the

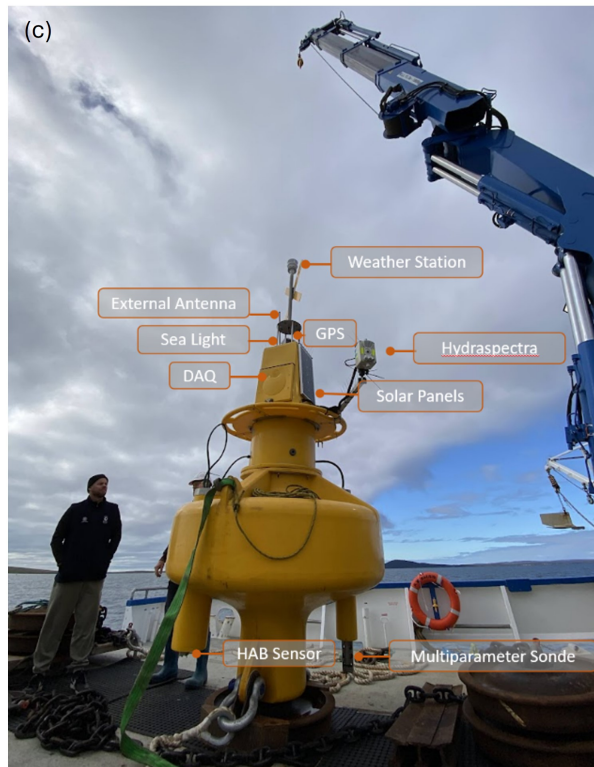
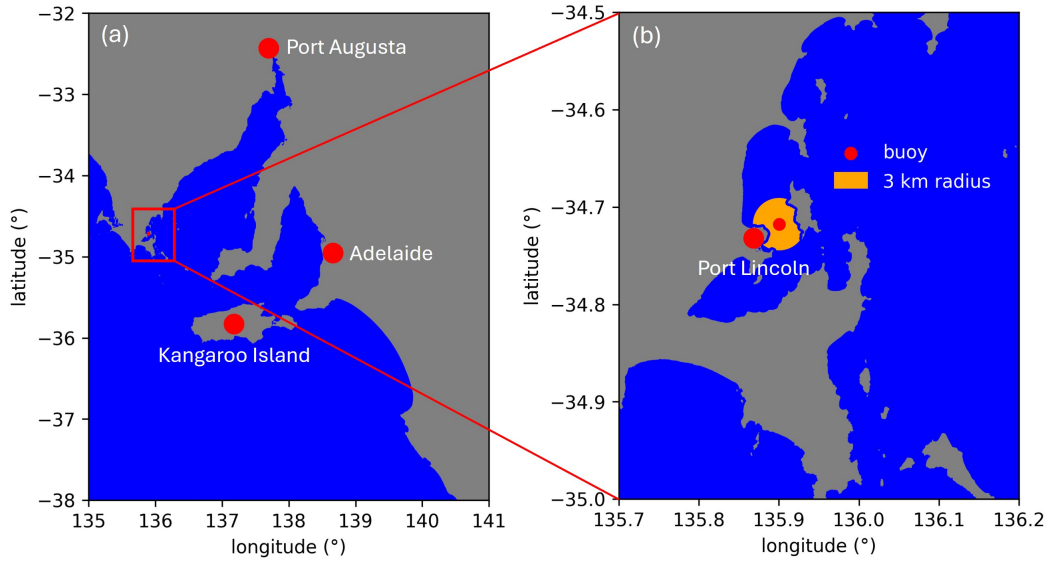


Figure 4. A buoy has been set up near Port Lincoln in this study to collect in-situ sea surface temperature (SST) for validating the satellite-derived SST data. (a) Location of the buoy; (b) Zoomed-in view of the buoy location; and (c) A photo of the buoy before deployment.

spatiotemporal patterns of SST in the study area. In Subsection 3.2, we briefly review the well-established equations underlying the radiative transfer process from the water-emitted radiance to the sensor-captured top-of-atmosphere radiance. In Subsection 3.3,

we describe the derivation of atmospheric radiative variables via three radiative transfer simulations with the *libRadtran* software package [46]. We detail in Subsection 3.4 the calculation of atmospheric parameters from CAMS EAC4 atmosphere data which are required as inputs for the *libRadtran* simulations. Then, in Subsection 3.5, we calculate SST based on the radiative transfer equations and derived atmospheric radiative variables. In Subsection 3.6, we introduce a framework to parallelise the SST calculation for large spatiotemporal scales. Finally, we detail the methodologies for analysing the spatiotemporal patterns of SST, deriving the baseline SST climatology, and detecting anomalous SST events in Subsection 3.7.

3.2. Radiative Transfer Modelling

Figure 5 illustrates the radiative transfer process from sea surface radiance to at-sensor radiance, with interference from atmospheric scattering, absorption, and emission. As depicted in the figure, the emission of thermal infrared radiance from the surface of sea water, $\varepsilon(\lambda) \cdot L_s(\lambda)$, is a product of the black-body radiance of water $L_s(\lambda)$ (which is determined by sea surface temperature T through the Planck's law) and water emissivity $\varepsilon(\lambda)$, where λ denotes spectral dependency. The water-emitted radiance then passes through the atmosphere with a transmittance coefficient of $\tau(\lambda)$. Part of the radiation, $[1 - \tau(\lambda)] \cdot \varepsilon(\lambda) \cdot L_s(\lambda)$, is absorbed and scattered by atmospheric constituents such as water vapour and carbon dioxide. The remaining part, $\tau(\lambda) \cdot \varepsilon(\lambda) \cdot L_s(\lambda)$, reaches the top of atmosphere.

In addition to the water-emitted radiance, the atmosphere itself also emits radiation (Figure 5). The atmospheric upwelling radiance, $L_u(\lambda)$, is the radiant energy that is emitted or scattered upwards from the atmosphere. The atmospheric downwelling radiance, $L_d(\lambda)$, is that going downward, which is then partially absorbed by sea water ($\varepsilon(\lambda) \cdot L_d(\lambda)$) and the rest is re-emitted upward ($[1 - \varepsilon(\lambda)] \cdot L_d(\lambda)$). The re-emitted radiation then passes upward through the atmosphere, with part being absorbed and scattered ($[1 - \tau(\lambda)] \cdot [1 - \varepsilon(\lambda)] \cdot L_d(\lambda)$) and the rest reaching the top of atmosphere ($\tau(\lambda) \cdot [1 - \varepsilon(\lambda)] \cdot L_d(\lambda)$).

The total at-sensor radiance measurable by the thermal infrared instrument on-board the satellite, $L_t(\lambda)$, is the combination of water-emitted radiance and atmospheric

upwelling and downwelling radiances that reach the top of atmosphere. The entire radiative transfer process can be described mathematically as the following:

$$L_t(\lambda) = \tau(\lambda) \cdot \varepsilon(\lambda) \cdot L_s(\lambda) + L_u(\lambda) + \tau(\lambda) \cdot [1 - \varepsilon(\lambda)] \cdot L_d(\lambda), \quad (1)$$

where $L_s(\lambda)$ is the black-body radiance of sea water; $L_u(\lambda)$ and $L_d(\lambda)$ are atmospheric upwelling and downwelling radiances, respectively; $\tau(\lambda)$ is the transmittance of atmosphere; and $\varepsilon(\lambda)$ is the emissivity of sea water. The radiative transfer model in Eq. (1) establishes the forward relationship between the black-body radiance of sea water, $L_s(\lambda)$, and the at-sensor radiance, $L_t(\lambda)$.

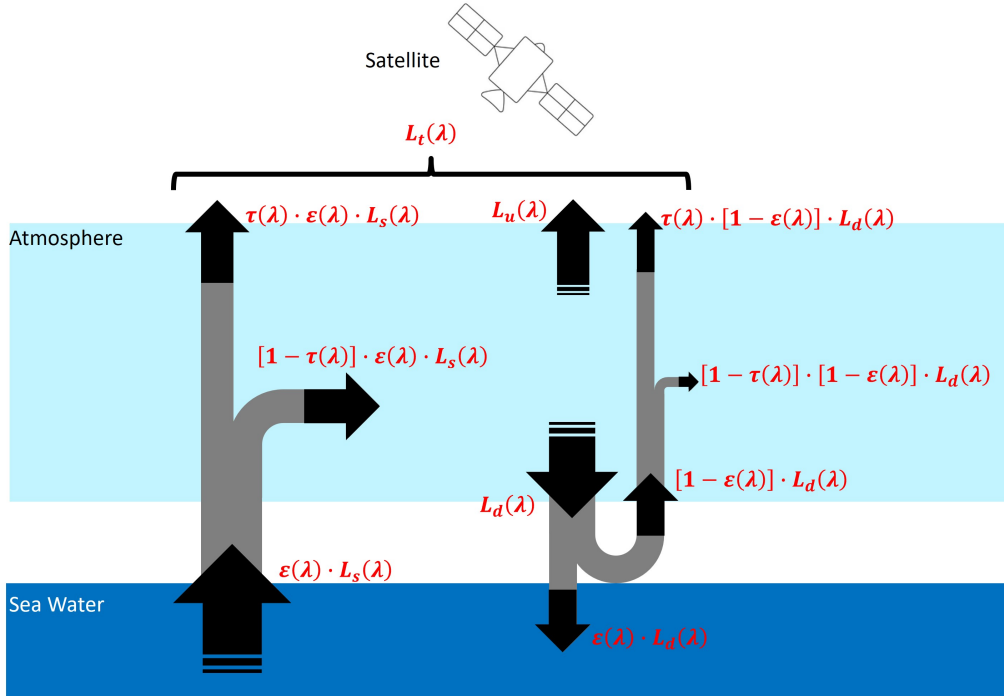


Figure 5. Simplified radiative transfer process from the radiance of sea water to at-sensor radiance, with interference from atmospheric scattering, absorption, and emission. $L_s(\lambda)$ is the black-body radiance of sea water; $L_t(\lambda)$ is the at-sensor radiance; $L_u(\lambda)$ and $L_d(\lambda)$ are atmospheric upwelling and downwelling radiances, respectively; $\tau(\lambda)$ is the transmittance of atmosphere; $\varepsilon(\lambda)$ is the emissivity of sea water; and λ denotes spectral dependency.

3.3. Derivation of Atmospheric Radiative/Transmission Variables

In Eq. (1) the three variables $\tau(\lambda)$, $L_u(\lambda)$, and $L_d(\lambda)$ characterise the radiative/transmission properties of atmosphere. Following the approach in [14], three at-

atmospheric simulations were conducted with the radiative transfer software package *libRadtran* [46], to derive these variables. It is worth noting that, these simulations were conducted under assumed atmospheric parameters for the purpose of solving the radiative transfer equation (Eq. (1)), rather than simulating with the actual atmospheric conditions.

In the first simulation, we assumed the spectral emissivity of water $\varepsilon(\lambda)$ to be 1 for all wavelengths, and the black-body radiance of water $L_s(\lambda)$ to be the spectral radiance of a 290 K black body. We noted the assumed $\varepsilon(\lambda)$ and $L_s(\lambda)$ values as $\varepsilon^{(1)}(\lambda)$ and $L_s^{(1)}(\lambda)$, respectively. Under such assumptions, Eq. (1) became:

$$\begin{aligned} L_t^{(1)}(\lambda) &= \tau(\lambda) \cdot \varepsilon^{(1)}(\lambda) \cdot L_s^{(1)}(\lambda) + L_u(\lambda) + \tau(\lambda) \cdot (1 - \varepsilon^{(1)}(\lambda)) \cdot L_d(\lambda) \\ &= \tau(\lambda) \cdot L_s^{(1)}(\lambda) + L_u(\lambda), \end{aligned} \quad (2)$$

where $L_t^{(1)}(\lambda)$ is the *libRadtran*-simulated at-sensor radiance under the $\varepsilon^{(1)}(\lambda)$ and $L_s^{(1)}(\lambda)$ assumptions.

In the second simulation, we assumed $\varepsilon(\lambda)$ to be 1 for all wavelengths and $L_s(\lambda)$ to be the spectral radiance of a 300 K black body, noted as $\varepsilon^{(2)}(\lambda)$ and $L_s^{(2)}(\lambda)$, respectively, and Eq. (1) became:

$$\begin{aligned} L_t^{(2)}(\lambda) &= \tau(\lambda) \cdot \varepsilon^{(2)}(\lambda) \cdot L_s^{(2)}(\lambda) + L_u(\lambda) + \tau(\lambda) \cdot (1 - \varepsilon^{(2)}(\lambda)) \cdot L_d(\lambda) \\ &= \tau(\lambda) \cdot L_s^{(2)}(\lambda) + L_u(\lambda), \end{aligned} \quad (3)$$

where $L_t^{(2)}(\lambda)$ is the corresponding *libRadtran*-simulated at-sensor radiance under the $\varepsilon^{(2)}(\lambda)$ and $L_s^{(2)}(\lambda)$ assumptions. By combining Eqs (2) and (3), the transmittance of atmosphere $\tau(\lambda)$ and atmospheric upwelling radiance $L_u(\lambda)$ were derived as:

$$\tau(\lambda) = \frac{L_t^{(2)}(\lambda) - L_t^{(1)}(\lambda)}{L_s^{(2)}(\lambda) - L_s^{(1)}(\lambda)}, \quad (4)$$

$$L_u(\lambda) = L_t^{(1)}(\lambda) - \frac{L_t^{(2)}(\lambda) - L_t^{(1)}(\lambda)}{L_s^{(2)}(\lambda) - L_s^{(1)}(\lambda)} \cdot L_s^{(1)}(\lambda). \quad (5)$$

In the third simulation, we assumed $\varepsilon(\lambda)$ to be 0.95 and $L_s(\lambda)$ to be 0 (*i.e.*, equivalent to black-body radiance at 0 K), noted as $\varepsilon^{(3)}(\lambda)$ and $L_s^{(3)}(\lambda)$, respectively. Then Eq. (1) became:

$$\begin{aligned} L_t^{(3)}(\lambda) &= \tau(\lambda) \cdot \varepsilon^{(3)}(\lambda) \cdot L_s^{(3)}(\lambda) + L_u(\lambda) + \tau(\lambda) \cdot [1 - \varepsilon^{(3)}(\lambda)] \cdot L_d(\lambda) \\ &= L_u(\lambda) + \tau(\lambda) \cdot [1 - \varepsilon^{(3)}(\lambda)] \cdot L_d(\lambda), \end{aligned} \quad (6)$$

where $L_t^{(3)}(\lambda)$ is the corresponding *libRadtran*-simulated at-sensor radiance under the $\varepsilon^{(3)}(\lambda)$ and $L_s^{(3)}(\lambda)$ assumptions. Taking into consideration of Eqs (4), (5), and (6), the atmospheric downwelling radiance $L_d(\lambda)$ was derived as:

$$L_d(\lambda) = \frac{L_t^{(3)}(\lambda) - L_t^{(1)}(\lambda) + \frac{L_t^{(2)}(\lambda) - L_t^{(1)}(\lambda)}{L_s^{(2)}(\lambda) - L_s^{(1)}(\lambda)} \cdot L_s^{(1)}(\lambda)}{[1 - \varepsilon^{(3)}(\lambda)] \cdot \frac{L_t^{(2)}(\lambda) - L_t^{(1)}(\lambda)}{L_s^{(2)}(\lambda) - L_s^{(1)}(\lambda)}}. \quad (7)$$

It is worth noting that the three *libRadtran* simulations were conducted for the thermal spectral range from 9,000 nm to 14,050 nm at 1 nm spectral sampling interval. Therefore, the derived $\tau(\lambda)$, $L_u(\lambda)$, and $L_d(\lambda)$, based on Eqs (4), (5), and (7), respectively, were of the same spectral range (9,000–14,050 nm) and interval (1 nm).

3.4. Calculation of Atmospheric Parameters

The parameters of atmospheric conditions (*e.g.*, air pressure, temperature, and relative humidity) were required as inputs for the three *libRadtran* simulations in Subsection 3.3. Instead of applying a standard mid-latitude summer or winter atmosphere as the default atmospheric conditions, we chose to make use of spatiotemporally specific atmospheric conditions when and where the satellite observation was captured. Considering that accurate atmospheric corrections are critical in SST retrieval, location- and time-specific atmospheric conditions may help improve the quality of the retrieved SST values.

In this study, we used the CAMS EAC4 atmosphere data to derive spatiotemporally specific atmospheric conditions for each satellite observation. Considering that the spatial resolution of the CAMS EAC4 dataset is 0.75 degree longitude by 0.75 degree

latitude and the temporal resolution is 3 hours, we divided the satellite image archive of interest into a spatiotemporal grid with each cell in the grid covering images over an area of 0.75 degree longitude by 0.75 degree latitude and a time period of 3 hours (as detailed later in Subsection 3.6).

For each cell, the corresponding mean sea level air pressure (single level value at sea surface, in Pa) was retrieved from the CAMS EAC4 data set. It was then converted from the single level air pressure at sea surface, to the vertical profile of air pressure at 60 discretised levels (from sea surface to top of atmosphere), based on the 60-level vertical discretisation model as defined in [47] and the converting coefficients for each model level as provided in CAMS EAC4:

$$p^{(i)} = a^{(i)} + p_0 \cdot b^{(i)} \quad (8)$$

where p_0 is the air pressure at sea surface; $p^{(i)}$ is the air pressure at the i th model level; and $a^{(i)}$ and $b^{(i)}$ are the corresponding converting coefficients for that model level.

Cell-specific retrievals of atmosphere conditions from the CAMS EAC4 data set also included air temperature $T^{(i)}$ (in unit of K), specific humidity $q^{(i)}$ (in unit of kg/kg), ozone concentration $O_3^{(i)}$ (in unit of kg/kg), and nitrogen dioxide concentration $NO_2^{(i)}$ (in unit of kg/kg). All these parameters were provided as vertical profiles at the 60 model levels from sea surface to top of atmosphere, with i ranging from 1 to 60 in their notations.

The altitude of each model level was calculated from the air pressure at sea surface p_0 and the vertical profiles of air pressure $p^{(i)}$ and air temperature $T^{(i)}$ via the Barometric formula:

$$h^{(i)} = -\frac{\ln\left(\frac{p^{(i)}}{p_0}\right) \cdot R \cdot T^{(i)}}{g \cdot M} + h_0, \quad (9)$$

where $h^{(i)}$ is the altitude at the i th model level; $h^{(i)}=0$ m is the altitude of sea surface; $g=9.8067$ m/s² is the gravitational acceleration; $R=8.31446$ J/(K · mol) is the universal gas constant; and $M^{(i)}$ is the molar mass of air at the i th model level, which was

calculated as the combination of molar mass of dry air and water vapour weighted by the specific humidity of the same model level $q^{(i)}$:

$$M^{(i)} = M_d \cdot (1 - q^{(i)}) + M_v \cdot q^{(i)}, \quad (10)$$

where $M_d=0.0289652$ kg/mol and $M_v=0.018016$ kg/mol are the molar mass of dry air and water vapour, respectively.

The air density $\rho^{(i)}$ at the i th model level was calculated based on the Ideal Gas Law by treating the atmosphere as a mixture of dry air and water vapour:

$$\rho^{(i)} = \frac{p_d^{(i)} \cdot M_d + p_v^{(i)} \cdot M_v}{R \cdot T^{(i)}}, \quad (11)$$

where $p_d^{(i)}$ and $p_v^{(i)}$ are the partial pressure of dry air and water vapour, respectively, at the i th model level. The water vapour pressure $p_v^{(i)}$ was calculated as [43, 44]:

$$p_v^{(i)} = \frac{q^{(i)} \cdot p^{(i)}}{\frac{M_v}{M_d} + \left(1 - \frac{M_v}{M_d}\right) \cdot q^{(i)}}, \quad (12)$$

where $p^{(i)}$ is air pressure and $q^{(i)}$ is specific humidity at the i th model level, both of which were provided by CAMS EAC4. Given $p_v^{(i)}$, the dry air pressure $p_d^{(i)}$ can be calculated as:

$$p_d^{(i)} = p^{(i)} - p_v^{(i)}. \quad (13)$$

Nitrogen (N_2), oxygen (O_2), and carbon dioxide (CO_2) constitute 75.523%, 23.133%, and 0.053%, respectively, of dry air by mass ratio (*i.e.*, in unit of kg/kg). Although the compositions of these gasses in dry air don't change with altitude, their compositions in total air do due to the vertical variations of water vapour content. To this end, the nitrogen concentration $N_2^{(i)}$ (in unit of kg/kg), oxygen concentration $O_2^{(i)}$ (in unit of kg/kg), and carbon dioxide concentration $CO_2^{(i)}$ (in unit of kg/kg) at the i th model level were calculated with the specific humidity of that model level $q^{(i)}$ being

considered:

$$N_2^{(i)} = (1 - q^{(i)}) \times 0.75523, \quad (14)$$

$$O_2^{(i)} = (1 - q^{(i)}) \times 0.23133, \quad (15)$$

$$CO_2^{(i)} = (1 - q^{(i)}) \times 0.00053, \quad (16)$$

In summary, for each cell that covers a spatial span of 0.75 degree longitude by 0.75 degree latitude and a temporal span of 3 hours, the spatiotemporally specific atmosphere variables, including air pressure $p^{(i)}$, air temperature $T^{(i)}$, air density $\rho^{(i)}$, water vapour content $q^{(i)}$, nitrogen concentration $N_2^{(i)}$, oxygen concentration $O_2^{(i)}$, and carbon dioxide concentration $CO_2^{(i)}$, ozone concentration $O_3^{(i)}$, and nitrogen dioxide concentration $NO_2^{(i)}$, at 60 model levels from sea surface to the top of atmosphere, were provided as inputs to the *libRadtran* simulations detailed in Subsection 3.3.

3.5. Calculation of SST

After determining the atmospheric radiative variables, *i.e.*, $\tau(\lambda)$, $L_u(\lambda)$, and $L_d(\lambda)$, with the *libRadtran* simulations described in Subsection 3.3, we convolved these spectral quantities with the TIRS spectral response functions to convert them into broadband quantities that match with TIRS Band 10 (10.60–11.19 μm) and Band 11 (11.50–12.51 μm). We denote these broadband atmospheric radiative variables as τ^{B10} , L_u^{B10} , and L_d^{B10} for Band 10, and τ^{B11} , L_u^{B11} , and L_d^{B11} for Band 11. By convolving a lab measurement of the spectral emissivity of sea water with TIRS spectral response functions, the broadband emissivity of sea water at TIRS Bands 10 and 11 were determined to be $\epsilon^{\text{B10}} = 0.9926$ and $\epsilon^{\text{B11}} = 0.9877$, as documented in [14]. Then, deriving from Eq. (1),

the black-body radiance of sea water at Band 10, L_s^{B10} , can be calculated as:

$$L_s^{\text{B10}} = \frac{L_t^{\text{B10}} - L_u^{\text{B10}}}{\tau^{\text{B10}} \cdot \varepsilon^{\text{B10}}} - \frac{(1 - \varepsilon^{\text{B10}}) \cdot L_d^{\text{B10}}}{\varepsilon^{\text{B10}}}, \quad (17)$$

where L_s^{B10} is the at-sensor radiance recorded by TIRS Band 10. The same calculation can be applied to get the black-body radiance of sea water at Band 11, L_s^{B11} .

The SST can be retrieved from either L_s^{B10} or L_s^{B11} based on the physical relationship between black-body radiance and temperature, as described by Planck's Law. In this study, SST was calculated as the average over the retrievals from both bands:

$$T = \frac{1}{2} \left[\frac{K_2^{\text{B10}}}{\ln \left(\frac{K_1^{\text{B10}}}{L_s^{\text{B10}}} + 1 \right)} + \frac{K_2^{\text{B11}}}{\ln \left(\frac{K_1^{\text{B11}}}{L_s^{\text{B11}}} + 1 \right)} \right] - 273.15, \quad (18)$$

where T is the derived SST in degree Celsius ($^{\circ}\text{C}$); $K_1^{\text{B10}} = 774.8853$, $K_2^{\text{B10}} = 1321.0789$, $K_1^{\text{B11}} = 480.8883$, and $K_2^{\text{B11}} = 1201.1442$ are sensor-specific constants as documented in Landsat 8 Data Users Handbook [48]. It is worth noting that the SST values derived here represent the skin temperature of the water surface. To validate them against the bulk temperatures measured by in-situ sensors, the skin temperatures were compared with in-situ bulk temperature measurements over two years for the Port Lincoln buoy, and over 2.5 years for the New South Wales buoys. An offset of 0.6°C was applied to the Port Lincoln buoy and 0.9°C to the New South Wales buoys, to account for the difference between skin and bulk temperatures.

3.6. Parallelisation for Large-Scale Processing

Given the spatiotemporal scale of this study, we divided the study area into multiple tiles to facilitate parallelised and efficient processing. Each tile encompasses a $0.75^{\circ} \times 0.75^{\circ}$ longitude/latitude area, with its centre aligned to the sampling point of the CAMS EAC4 atmospheric data, as illustrated in Figure 6. Multitemporal TIRS images from 2014 to 2023 were extracted and processed independently for each tile. For efficiency, only the tiles intersecting the study area were processed, while water tiles outside the study area and pure-land tiles were skipped. These tiles were distributed across the

workers of a Dask cluster on Amazon Web Services within CSIRO's EASI platform. Please refer to the Data Availability section for details on data access.

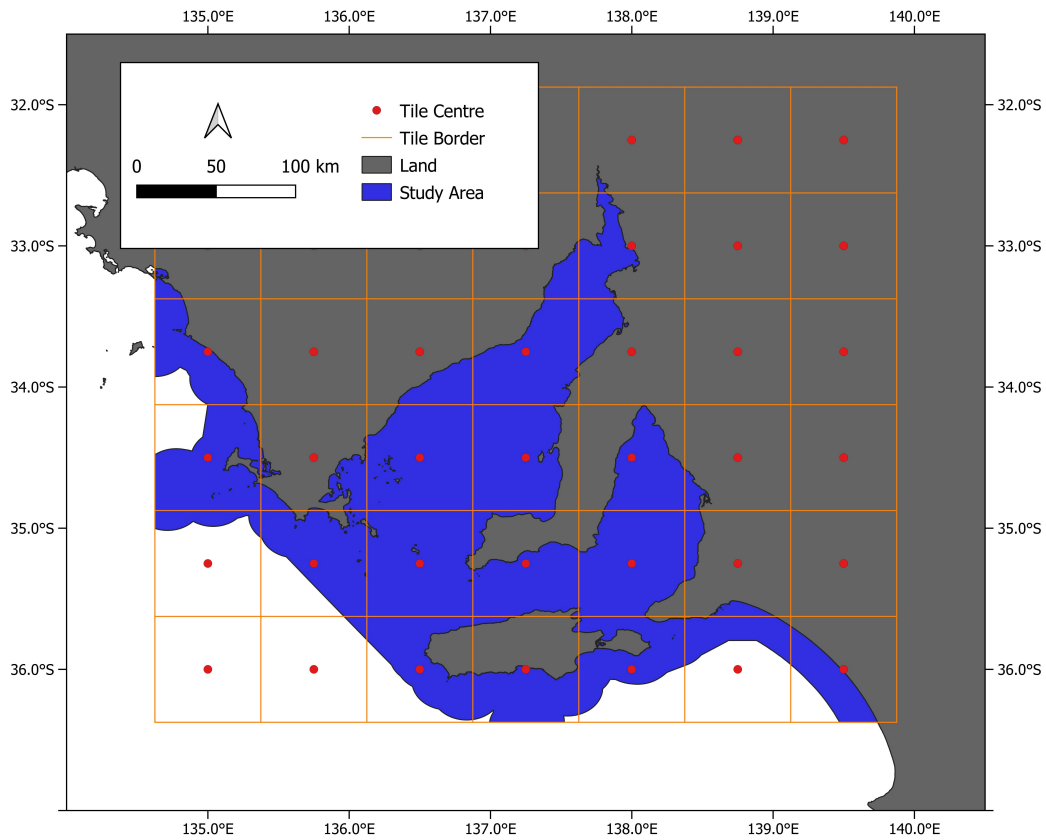


Figure 6. The study area is divided into $0.75^{\circ} \times 0.75^{\circ}$ lon/lat tiles for accelerated and efficient processing, where the tile centres align with the sampling points of CAMS EAC4 atmosphere data.

3.7. Spatiotemporal Analyses

To analyse the spatiotemporal patterns of SST in the study area, we computed the mean SST and coefficient of variation (C.V.) of SST from 2014 to 2023. These metrics allowed us to identify spatial patterns in SST levels across the study area as well as areas with high temporal variability. Monthly SST maps were also generated to capture seasonal temperature fluctuations. This analysis aimed to provide seasonal information on SST for supporting the local fishery and aquaculture industries.

The baseline climatology of SST was extracted for each calendar date with the ten years of SST imagery (2014–2023) derived in this study. Specifically, for each pixel, we first amalgamated SST observations from all years into one single calendar year based

on their acquisition day of the year, followed by fitting these observations to a sinusoidal function expressed as:

$$T(d) = A \cdot \cos\left(\frac{2\pi d}{365} + \phi\right) + O, \quad (19)$$

where $T(d)$ is the SST observation at the d th calendar day of a year, and the amplitude A , phase ϕ , and offset O are parameters to be determined through fitting. Figure 7 illustrates the procedure of extracting the baseline climatology for a randomly selected pixel. This approach was applied to every pixel within the study area to generate the climatology maps.

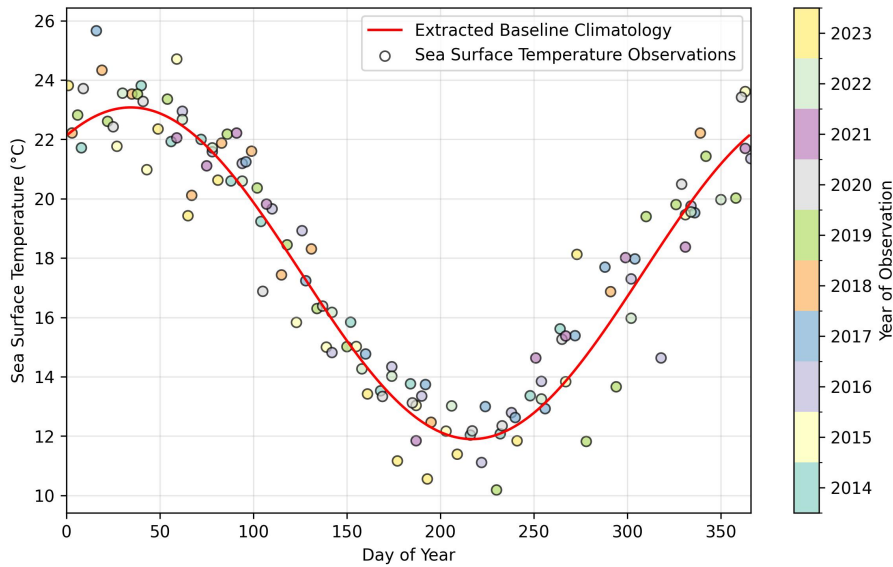


Figure 7. Demonstration of baseline climatology extraction for sea surface temperature (SST) at a randomly selected location (137.6°E, 33.4°S) within the study area.

With the baseline climatology, we calculated the probability map of anomalous temperatures in the study area, which is defined as the percentage of SST observations from 2014 to 2023 that are greater than or less than 2°C from the baseline temperature. This threshold was empirically determined based on observations reported in the literature, which indicate that a temperature offset exceeding 2°C may cause adverse impacts on marine species, such as increasing the risk of mass coral mortality [49]. However, anomaly maps can be generated under other threshold values following the same approach described here. Based on the anomaly map, regions with high probabilities of

anomalous SST were identified. To examine the seasonal distribution of SST anomalies, we further categorised the detected anomalous events by the warm months (January–March and October–December) and cool months (April–September), and compared the likelihood of SST events between these two seasons.

4. Results and Discussions

4.1. Validation of SST Retrievals

The time-series plot in Figure 8a shows the comparison between satellite-derived SST data and in-situ SST measurements collected at the location of Port Lincoln buoy (135°54'01"E, 34°43'03"S). It was observed that the satellite-derived SST values aligned well with the in-situ measurements. It was also seen that the overall temperature trends, including seasonal variations and peaks, were captured by the satellite-derived SST. The scatter plot in Figure 8b presents the relationship between the satellite-derived and in-situ SST. The quantitative assessment shows a reasonably strong correlation between the two, with an r^2 value of 0.97 and a root mean square error (RMSE) of 0.38°C. The results for the Batemans Bay Offshore Buoy (150°20'13"E, 35°42'28"S), Coffs Harbour Offshore Buoy (153°15'32"E, 30°22'22"S), and Crowdy Head Offshore Buoy (152°51'08"E, 31°49'26"S) are shown in Figures 9a–b, 9c–d, and 9e–f, respectively. It was observed that the r^2 values are within the range of 0.85–0.90 and the RMSE values are lower than 0.75°C. The validation results in Figures 8 and 9 suggested that the SST retrievals obtained using the algorithm proposed in this study provide a reliable estimate of the temperature of sea surface waters.

4.2. Visualisation of SST Images

Figure 10 presents three randomly sampled SST images generated with the proposed workflow, alongside their aligning (*i.e.*, spatiotemporally coincident) true-colour images. The SST images in the left column revealed the thermal dynamics of sea surface waters, where cooler regions appear in blue and warmer areas in red. In Sample 1, an eddy was identified, likely indicating an upwelling event where colder, deeper waters rise to the

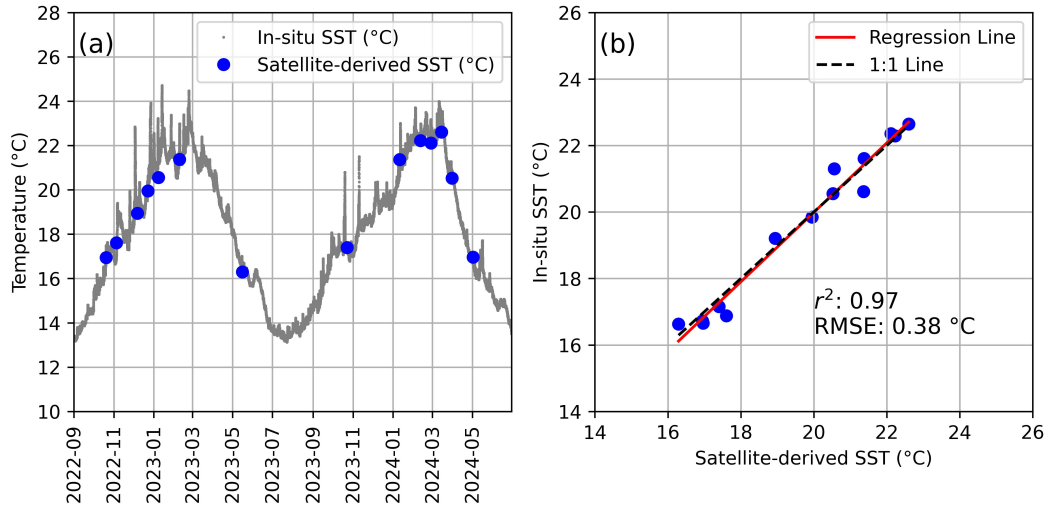


Figure 8. (a) Time-series comparison and (b) scatter plot between satellite-derived sea surface temperature (SST) and in-situ SST measurements collected at the location of the Port Lincoln buoy (135°54'01"E, 34°43'03"S).

surface. A thermal pattern was seen in Sample 2, with a sharp front in SST separating cooler and warmer water masses. From Sample 3, multiple smaller eddies were observed along a temperature gradient, indicating intricate mixing dynamics between warmer and cooler water masses. These thermal patterns reflect the underlying ocean circulation systems that distribute heat, nutrients, and energy in the marine system. While the SST images clearly depict these thermal features, they are less discernible in the aligning true-colour images shown in the right column of Figure 10. However, considering that optical images are valuable in estimating the concentrations of optically active water quality constituents, such as total suspended solids, coloured dissolved organic matter, and chlorophyll [50, 51], it would be worthwhile to synergise SST information with optical data to provide a comprehensive monitoring of marine systems.

Figure 11 compares the SST images recorded by the MODIS Terra sensor (Figure 11a) and derived in this study from the Landsat-8 TIRS observation (Figure 11b). Both images were captured on June 24, 2020, with a time difference of ~ 35 min, over waters surrounding the Jussieu Peninsula, South Australia. It was observed from the figure that both images shared a similar spatial pattern of SST, with a comparable range of SST values approximately between 10°C and 16°C . The MODIS Terra SST map (Figure 11a) displayed a relatively coarse spatial resolution (1000 m), with pixelated

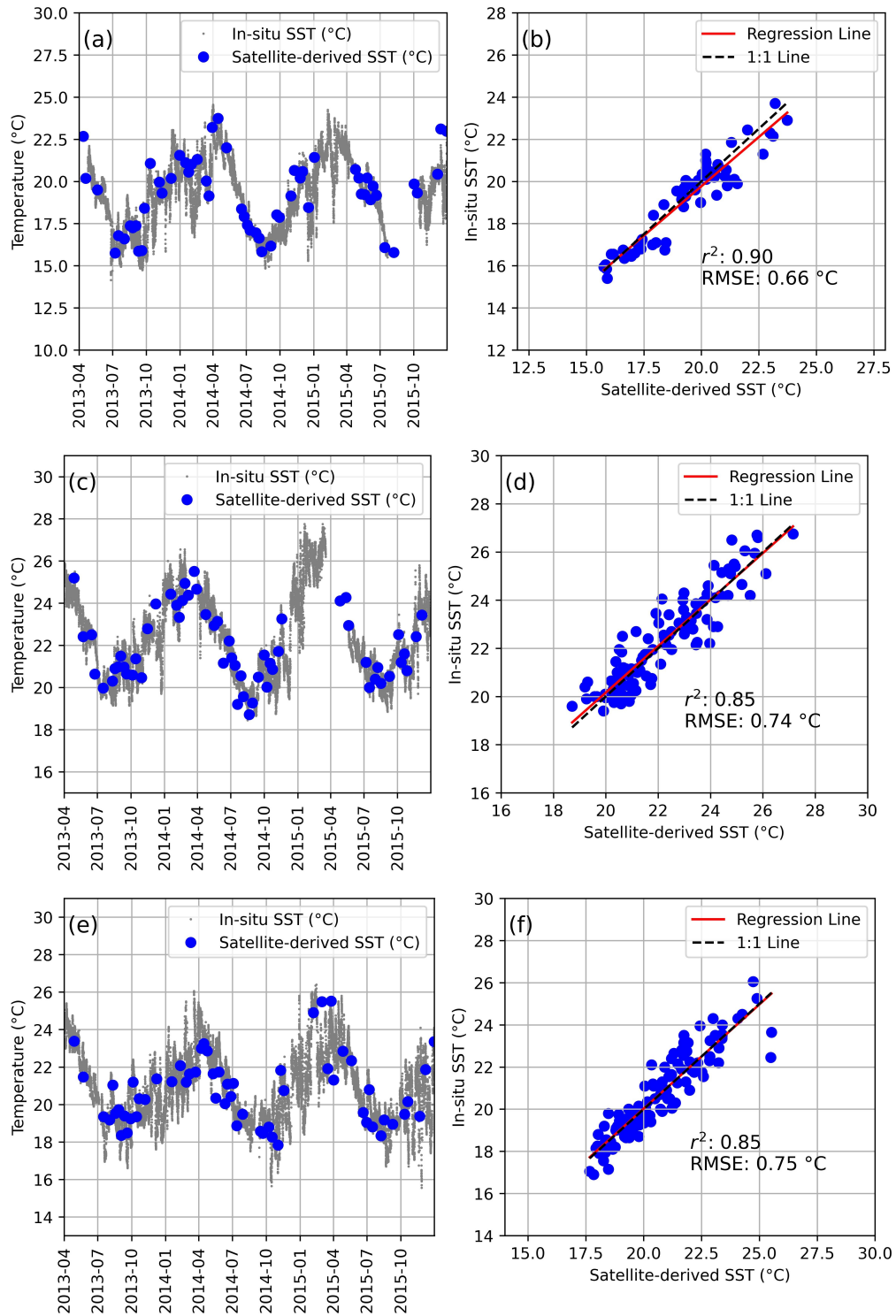


Figure 9. Time-series comparisons and scatter plots between satellite-derived sea surface temperature (SST) and in-situ SST measurements at (a–b) the Batemans Bay Offshore Buoy (150°20'13"E, 35°42'28"S), (c–d) Coffs Harbour Offshore Buoy (153°15'32"E, 30°22'22"S), and (e–f) Crowdy Head Offshore Buoy (152°51'08"E, 31°49'26"S).

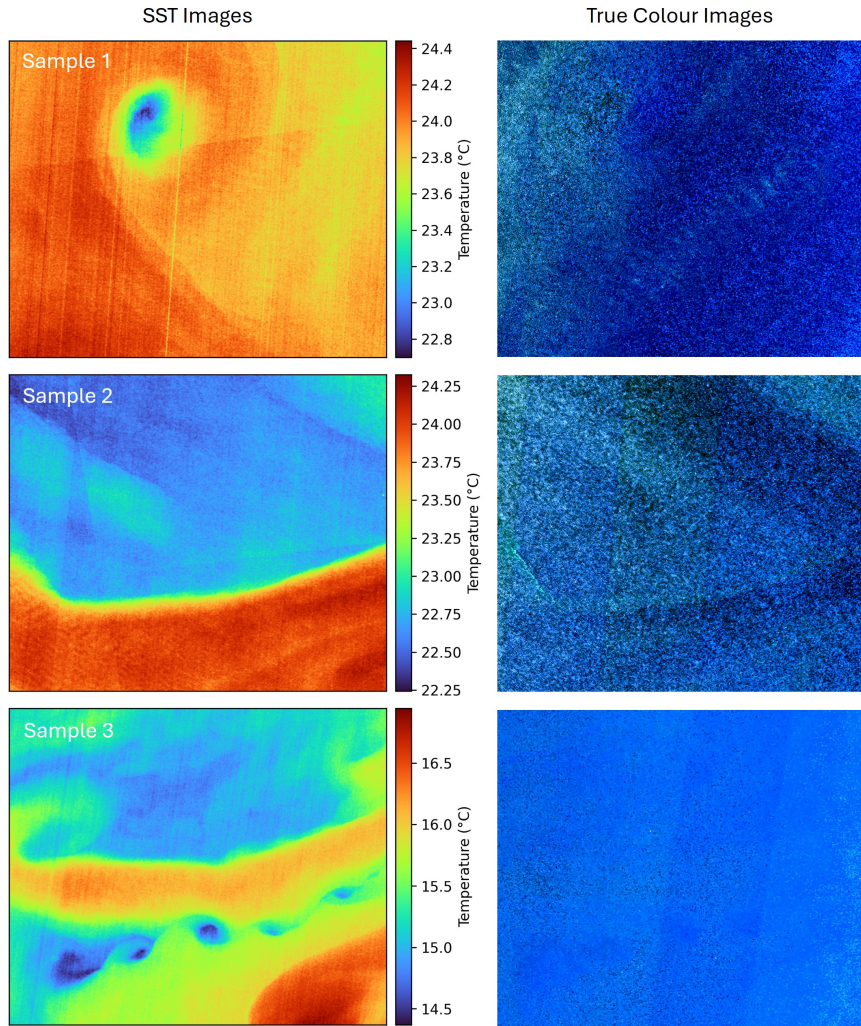


Figure 10. Three sample images of sea surface temperature (SST) generated with the proposed workflow (left column), and their spatiotemporally coincident true-colour images (right column).

regions showing distinct blocks of temperature values. In contrast, the SST map derived from Landsat-8 TIRS (Figure 11b) showed a finer spatial resolution (100 m), displaying a smoother, more continuous temperature gradient, which highlighted smaller-scale thermal features that were less resolved in the MODIS data.

4.3. Spatiotemporal SST Patterns

The spatial distribution of mean SST and the coefficient of variation (C.V.) of SST from 2014 to 2023 are shown in Figure 12. For the mean SST map (Figure 12a), it was seen that the mean temperature in the study area ranges from $\sim 14^{\circ}\text{C}$ to $\sim 20^{\circ}\text{C}$. Warmer

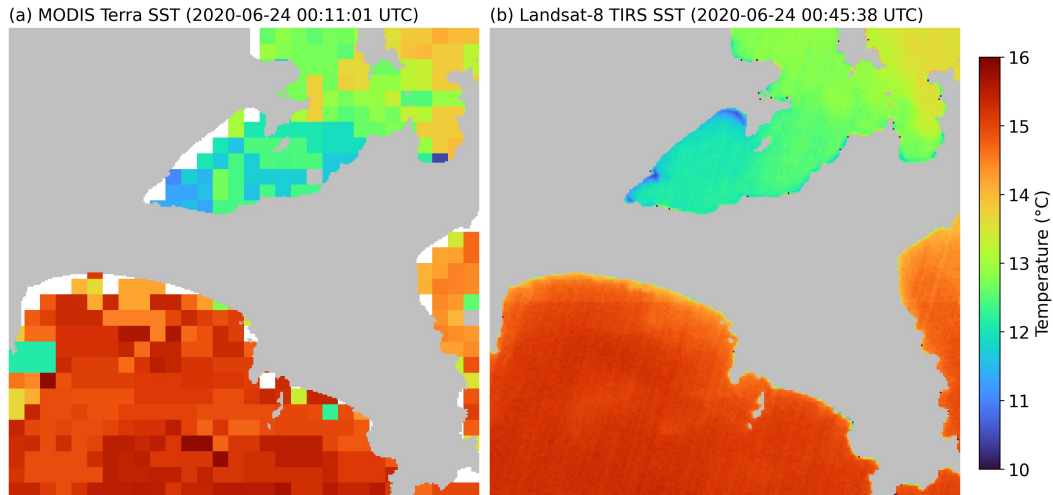


Figure 11. Comparison between the sea surface temperature (SST) images (a) recorded by the MODIS Terra sensor (1000 m resolution) and (b) derived in this study from Landsat-8 TIRS observations (100 m resolution).

waters were observed along the northern coastline, in particular for the Upper Spencer Gulf and Upper St Vincent Gulf regions, while cooler waters were seen in southern areas closer to the open ocean. The temporal variability of SST is illustrated in the C.V. map of SST (Figure 12b). Areas with high C.V. were observed in the Upper Spencer Gulf and Upper St Vincent Gulf regions, suggesting significant temporal variability in these areas. In contrast, the southern areas exhibited lower C.V. values, indicating more stable temperature conditions over time. The spatial distribution of SST and its temporal variability patterns, as given in Figure 12, could inform the local fishery and aquaculture industries for better practices, as the SST plays a key role in influencing the distribution, reproduction, and growth rates of marine species.

Figure 13 presents monthly SST maps in the study area, showing the seasonal variability of SST in the study region. A clear cycle of annual warming/cooling was observed, with the warmest temperatures occurring in the summer months (December to March) and the coolest during the winter months. In the summer period, the Upper Spencer Gulf and Upper St Vincent Gulf were observed to have the highest SST values, reaching over 26°C. This warming was seen to be most prominent in the Upper Spencer Gulf and Upper St Vincent Gulf regions close to the coastline. Cooler values were observed during the winter months, especially in July and August, where large portions of the study area exhibit temperatures below 14°C. In particular, the Upper Spencer

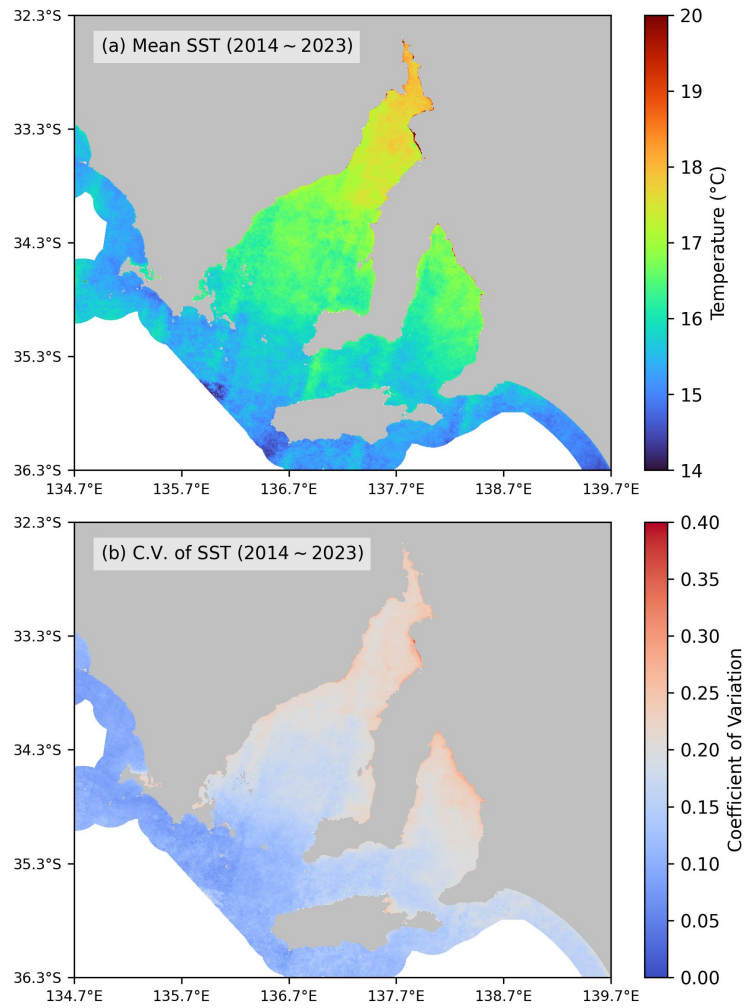


Figure 12. (a) The spatial distribution of mean sea surface temperature (SST) averaged over 2014–2023, and (b) the coefficient of variation (C.V.) of SST over the same time period.

Gulf and Upper St Vincent Gulf showed cooler temperatures than southern areas closer to the open ocean. The observation from Figure 13 that the Upper Spencer Gulf and Upper St Vincent Gulf regions showed higher temperatures during summer and lower temperatures during winter explains their higher C.V. values than the southern regions, as depicted in Figure 12b. Given that previous studies suggested that restricted water exchange and shallow bathymetry in semi-enclosed bays could lead to more rapid change in SST (*e.g.*, [52–54]), the higher summer SST and lower winter SST in Upper Spencer Gulf and Upper St Vincent Gulf could be attributed to those factors. By comparing the monthly mean SST maps, Figure 13 demonstrates the distinct seasonal SST cycle and its spatial variation. These seasonal patterns are essential for understanding marine

ecosystem dynamics and managing fisheries and aquaculture industries that rely on these temperature-dependent environments.

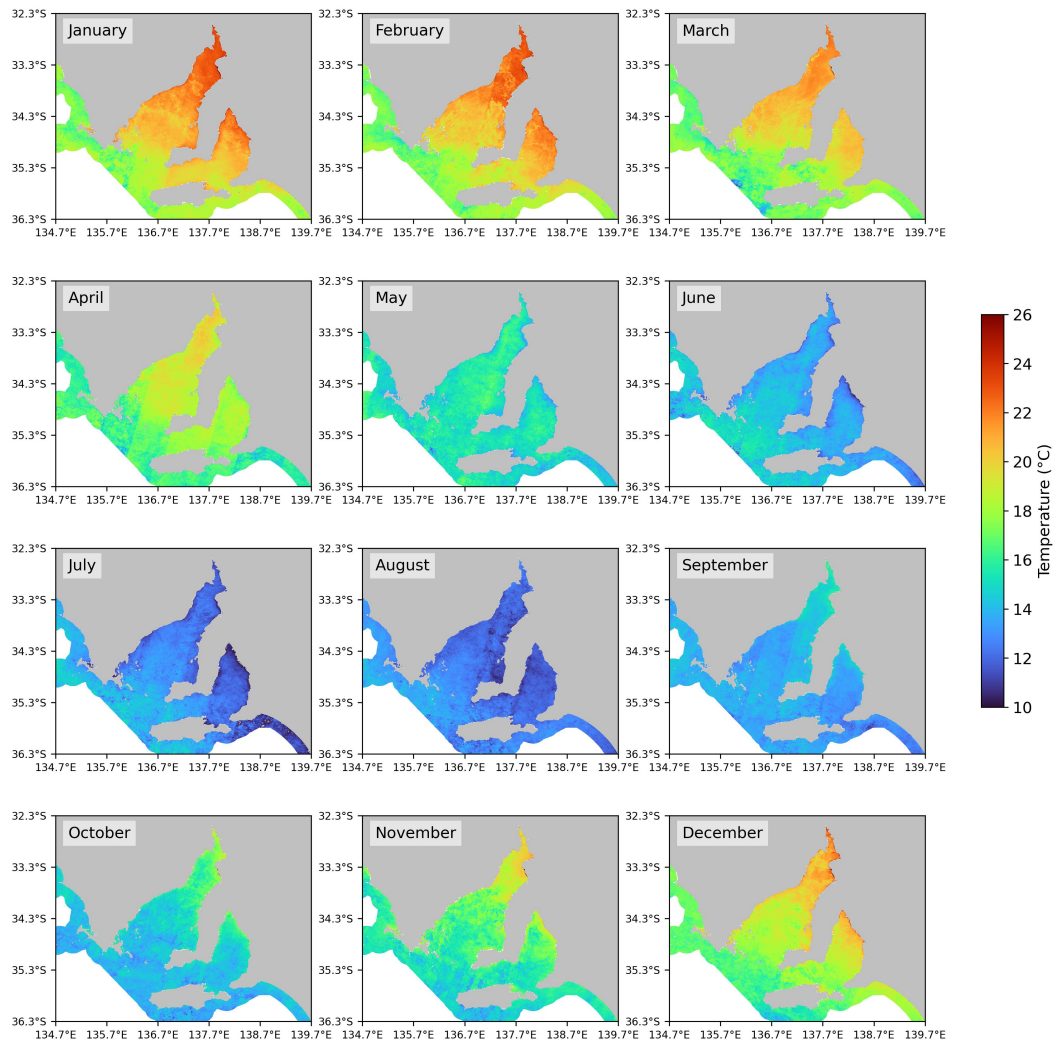


Figure 13. Monthly averages of sea surface temperature (SST) in the study area.

4.4. Daily Baseline Climatology

The baseline climatology of SST in the study area is shown in Figure 14. It is worth noting that, due to space constraints, only weekly interval climatology images are shown in the figure, while daily interval climatology images are available via the link provided in the Data Availability section. It was observed from Figure 14 that the climatology follows an annual warming and cooling cycle. Consistent with findings from the monthly mean SST maps in Figure 13, the semi-enclosed coastal waters of the gulfs display more

pronounced seasonal swings in the SST baseline climatology in Figure 14, as compared with the open southern regions.

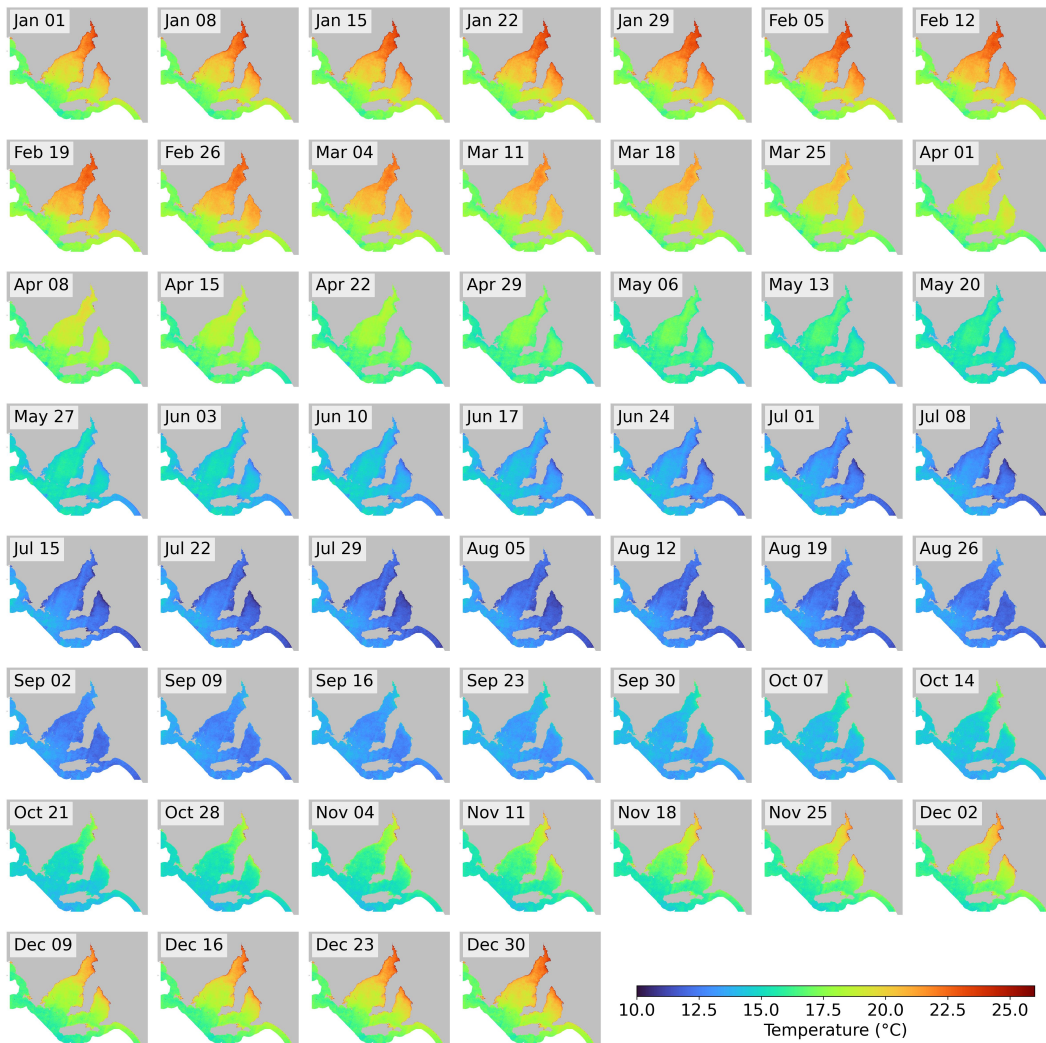


Figure 14. Annual baseline climatology of sea surface temperature (SST). Due to space constraints, only weekly interval climatology images are shown here. For access to daily interval climatology images, please refer to the Data Availability section.

The SST climatology data derived in this study incorporates the baseline spatiotemporal distribution of SST patterns with a spatial resolution of 100 m and a temporal resolution of 1 day. In terms of spatial resolution, it is higher than commonly used SST climatology data sets, such as the SSTAARS climatology data with 2 km resolution [28]. Therefore, it allows examining the SST climatology in finer spatial details, especially for near-shore coastal waters where the high spatial resolution near the coastline may reduce the possibility of mixed pixels and reveal small-scale SST features induced

by land-water interactions.

It is important to note that the Landsat-8 satellite passes over the study area at approximately 10:00 am local time, meaning that the daily peak/valley temperatures would be missed by the observations due to diurnal warming/cooling. Recalibration of the present climatology data would be necessary to obtain accurate baseline SST values for other times of the day.

4.5. SST Anomalies

Figure 15 shows the probability of anomalous temperatures in the study area, calculated as the percentage of SST observations from 2014 to 2023 that are greater than or less than 2°C from the baseline climatology. The highest probabilities of anomalous temperatures were observed in the near-shore waters of Upper Spencer Gulf and Upper St Vincent Gulf, with the probability higher than 40% (Figure 15). The high rate of SST anomalies in these areas may be explained by the shallow depth of water. Shallow waters experience more rapid and extreme temperature fluctuations than deeper waters because their lower thermal inertia allows them to quickly heat up and cool down in response to sudden changes in solar radiation and atmospheric temperature, as documented in studies of the Gulf of California [53] and Long Island Sound, New York [54]. The restricted water circulation in Upper Spencer Gulf and Upper St Vincent Gulf may also play a role, as limited mixing with open ocean waters can lead to localised warming or cooling—a phenomenon also observed in a study of Hawaii coastal waters [52]. These combined factors make the near-shore, shallow areas in Upper Spencer Gulf and Upper St Vincent Gulf particularly prone to anomalous SST conditions.

Figure 15 also reveals medium probabilities of SST anomalies in several isolated areas within the study region, particularly around Kangaroo Island. This pattern aligns with the high cloud coverage observed over these waters, as evidenced in Figure 2b. Given that cloud cover is identified as a factor contributing to variations in sea temperature [55], the high frequency of cloud coverage may play a role in the increased likelihood of anomalous SST events in these waters.

To analyse seasonal patterns of SST anomalies, we categorised the anomalous events by the warm months (January–March and October–December) and cool months

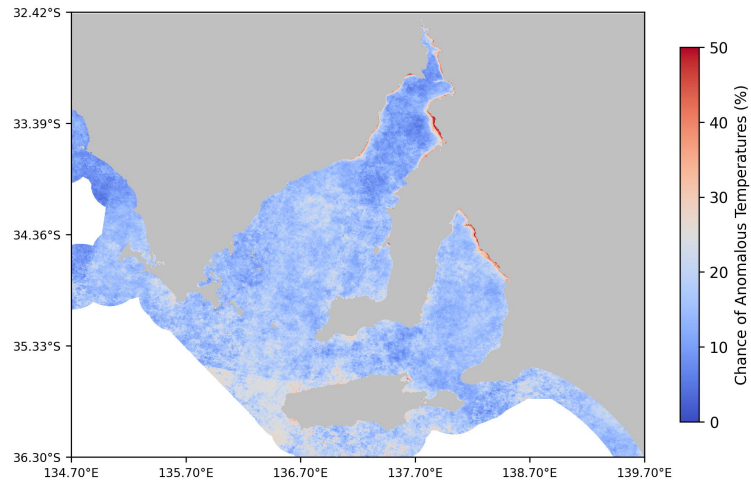


Figure 15. The probability of anomalous sea surface temperature (SST) observations in the study area. An anomaly is defined as an observed SST that is 2°C higher or lower than the baseline climatology.

(April–September), as shown in Figure 15. The analysis revealed that most anomaly events occurred during the warm season (Figure 15a), such as those detected in the the near-shore areas in Upper Spencer Gulf and Upper St Vincent Gulf, and those surrounding the Kangaroo Island. In comparison, the cool season experienced a lower rate of SST anomalies (Figure 15b). These findings suggest that SST during the warm season is more likely to deviate from the baseline climatology than the cool season, indicating more intense/frequent temperature fluctuations during warmer months like summer when the water column is more stratified.

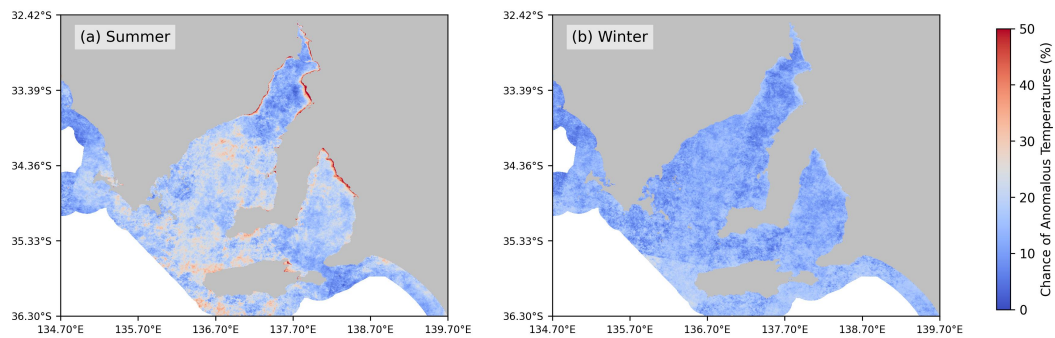


Figure 16. The probability of anomalous sea surface temperature (SST) observations in the study area during (a) summer months (January–March and October–December), and (b) winter months (April–September). An anomaly is defined as an observed SST that is 2°C higher or lower than the baseline climatology.

4.6. Limitations and Prospects

In this study, we presented an operational method for retrieving SST from the TIRS sensor. We then introduced a novel algorithm for constructing a daily SST climatology, which served as a baseline for identifying anomalous SST events. These methods were applied to temperate coastal waters in South Australia over a ten-year period from 2014 to 2023. While the results demonstrated the potential of Landsat-8 TIRS in high-resolution SST monitoring, there are some limitations and several opportunities for future improvements.

Firstly, this study utilised the Landsat-8 TIRS sensor due to its relatively high spatial resolution (100 m) and over ten years of historical data. This enabled a detailed, long-term analysis of SST in South Australia’s coastal waters. Despite its advantages, Landsat-8 TIRS has a relatively large revisit time of 16 days, and cloud cover may potentially extend data gaps even further. Integrating SST information derived from other satellite sensors, such as Sentinel-3 SLSTR [25], MODIS [23], and VIIRS [24], could help mitigate data gaps and enhance the temporal resolution, although the lower spatial resolutions of these sensor (750 m–1 km) may present an additional challenge for identifying small-scale SST features. The more recently launched TIRS-2 instrument [56] onboard Landsat-9 could be leveraged as an additional source of SST data.

Secondly, this work focused on monitoring the thermal state of coastal waters. In order to provide an enhanced monitoring of South Australia’s coastal environment, it is worth exploring in future studies the synergisation of the thermal observations with information recorded by optical sensors, such as the multispectral instruments Landsat-8 OLI [50, 57], Sentinel-2 MSI [58, 59] and Sentinel-3 OLCI [58], and the hyperspectral instruments PACE [60], Tanager [61], EnMAP [62], and DESIS [63, 64]. In addition, sea surface salinity, which can be measured using spaceborne L-band radiometers [65], can also be integrated to enhance insights into the mixing dynamics of fresh and seawater.

Thirdly, this study focused on detecting historical SST anomaly events over the ten-year period from 2014–2023. These detected SST events provide important information on the spatiotemporal distribution of anomalies historically. Implementing real-time anomaly detection techniques, potentially using cloud-based processing platforms, could enable early warnings of significant SST deviations. Such advancements would be

beneficial for fisheries, aquaculture, and environmental management by allowing timely responses to anomalous temperature fluctuations that may impact marine ecosystems.

Finally, while this study focused on South Australia’s coastal waters, the proposed approach could be extended to broader geographic regions to support marine and climate research at larger scales. Our valuation results shown in Subsection 4.1 suggested that the proposed SST retrieval algorithm has the potential to be adapted to regions outside the study area. Applying this methodology to different coastal environments, including tropical and polar regions, would help with a more comprehensive validation of the proposed algorithm.

5. Conclusion

This study demonstrated the capability of Landsat-8 TIRS in monitoring SST patterns, climatology, and anomalies in temperate coastal waters off the coast of South Australia over a ten-year period from 2014 to 2023. By developing an operational SST retrieval approach and establishing a novel high-resolution daily SST climatology, we examined the spatiotemporal patterns of SST and identified regions prone to anomalous temperature events. The high-resolution SST climatology derived in this study represents an improvement over existing datasets, offering enhanced spatial detail for detecting fine-scale temperature variations in coastal waters.

Our results suggested that (1) satellite-derived SST data obtained through the proposed method closely matched in-situ measurements, with an RMSE of approximately 0.38°C ; (2) the Upper Spencer Gulf and Upper St Vincent Gulf, being semi-enclosed regions, experienced more pronounced seasonal temperature variations, with elevated temperatures in summer and lower temperatures in winter relative to open ocean waters; (3) near-shore shallow waters and areas around Kangaroo Island showed a greater likelihood of SST anomalies than other parts of the study area; and (4) anomalous SST events were more prevalent in the warmer months (January–March and October–December) than in the cooler months (April–September). We also showed that the proposed SST retrieval algorithm has the potential to be extended to temperate coastal waters beyond the study area.

These findings provide valuable insights into localised SST dynamics and their implications for fisheries, aquaculture, and marine ecosystem management in temperate coastal waters in South Australia. Future work could focus on integrating information derived from other satellite sensors, incorporating real-time anomaly detection, and extending the approach to broader geographic regions.

Data Availability

- The SST product generated in this study is accessible via the CSIRO AquaWatch Data Explorer at: <https://explorer.adias.aquawatchaus.space/products/sst>;
- The colour-rendered SST image data can be viewed interactively via the CSIRO AquaWatch Map Portal at: <https://map.adias.aquawatchaus.space/#share=s-eBIRT8TGHR8DsQjB>;
- The baseline SST climatology data at daily intervals can be viewed online at: <https://drive.google.com/file/d/103RAnCJBONSbCPdafa9XVIqm4o6qdOSw>.

Acknowledgements

This work is supported by Commonwealth Scientific and Industrial Research Organisation (CSIRO) AquaWatch Australia Mission, CSIRO AI4Missions, South Australian Research and Development Institute (SARDI), SmartSat CRC, CSIRO Data61, CSIRO Environment, CSIRO Space and Astronomy, CSIRO Earth Analytics Science and Innovation (EASI) platform, and CSIRO AquaWatch Data Service (ADS).

The authors sincerely thank Ms Gemma Kerrisk at CSIRO Environment for her assistance in in-situ data acquisition and preparation, and Dr Robert Woodcock and Mr Tisham Dhar at CSIRO Space and Astronomy for their support in data processing and indexing on the EASI ADS platform. The authors acknowledge the New South Wales Government Office of Environment and Heritage (OEH) for providing in-situ sea surface temperature data from the Manly Hydraulics Laboratory Waverider buoys.

Declaration of using generative artificial intelligence (AI) in the writing process. During the preparation of this manuscript, the authors utilised GPT-4o to

refine language and enhance readability. All AI-assisted content was carefully reviewed and edited as necessary, and the authors take full responsibility for the final version of the publication.

References

- [1] P. Minnett, A. Alvera-Azcárate, T. Chin, G. Corlett, C. Gentemann, I. Karagali, X. Li, A. Marsouin, S. Marullo, E. Maturi, *et al.*, *Half a century of satellite remote sensing of sea-surface temperature*, *Remote Sensing of Environment* 233 (2019), p. 111366.
- [2] J. Taylor and M. Feng, *A deep learning model for forecasting global monthly mean sea surface temperature anomalies*, *Frontiers in Climate* 4 (2022), p. 178.
- [3] S. Lee and M.S. Park, *Seamless monitoring of marine heatwaves: capability of gap-filled, geostationary satellite sea surface temperature data*, *GIScience & Remote Sensing* 62 (2025), p. 2447746.
- [4] R. Legeckis, *Application of synchronous meteorological satellite data to the study of time dependent sea surface temperature changes along the boundary of the Gulf Stream*, *Geophysical Research Letters* 2 (1975), pp. 435–438.
- [5] R. Legeckis, *Long waves in the eastern equatorial Pacific Ocean: A view from a geostationary satellite*, *Science* 197 (1977), pp. 1179–1181.
- [6] R. Legeckis, *A survey of worldwide sea surface temperature fronts detected by environmental satellites*, *Journal of Geophysical Research: Oceans* 83 (1978), pp. 4501–4522.
- [7] F. Zhao, W. Ma, J. Zhao, Y. Guo, M. Tariq, and J. Li, *Global retrieval of the spectrum of terrestrial chlorophyll fluorescence: First results with TROPOMI*, *Remote Sensing of Environment* 300 (2024), p. 113903.
- [8] Y. Guo, X. Jia, D. Paull, and J.A. Benediktsson, *Nomination-favoured opinion pool for optical-SAR-synergistic rice mapping in face of weakened flooding signals*, *ISPRS Journal of Photogrammetry and Remote Sensing* 155 (2019), pp. 187–205.
- [9] J. Yang, H. Zhang, Y. Guo, R. Donohue, T. McVicar, S. Ferrier, W. Müller, X. Lü, Y. Fang, X. Wang, *et al.*, *Trajectories of plant nitrogen availability globally during 1984–2022 uncovered by satellite-derived nitrogen stable isotope ratio* (2023).
- [10] M.A. Cane, A.C. Clement, A. Kaplan, Y. Kushnir, D. Pozdnyakov, R. Seager, S.E. Zebiak, and R. Murtugudde, *Twentieth-century sea surface temperature trends*, *Science* 275 (1997), pp. 957–960.

- [11] G.A. Vecchi and B.J. Soden, *Effect of remote sea surface temperature change on tropical cyclone potential intensity*, Nature 450 (2007), pp. 1066–1070.
- [12] A. Pisano, S. Marullo, V. Artale, F. Falcini, C. Yang, F.E. Leonelli, R. Santoleri, and B. Buongiorno Nardelli, *New evidence of Mediterranean climate change and variability from sea surface temperature observations*, Remote Sensing 12 (2020), p. 132.
- [13] B. Mohamed, O. Ibrahim, and H. Nagy, *Sea surface temperature variability and marine heatwaves in the Black Sea*, Remote Sensing 14 (2022), p. 2383.
- [14] Q. Vanhellemont, *Automated water surface temperature retrieval from Landsat 8/TIRS*, Remote Sensing of Environment 237 (2020), p. 111518.
- [15] J. Fu, C. Chen, B. Guo, Y. Chu, and H. Zheng, *A split-window method to retrieving sea surface temperature from Landsat 8 thermal infrared remote sensing data in offshore waters*, Estuarine, Coastal and Shelf Science 236 (2020), p. 106626.
- [16] S.T. Lee, Y.K. Cho, and D.j. Kim, *Immense variability in the sea surface temperature near macro tidal flat revealed by high-resolution satellite data (Landsat 8)*, Scientific Reports 12 (2022), p. 248.
- [17] Q. Vanhellemont, R.J. Brewin, P.J. Bresnahan, and T. Cyronak, *Validation of Landsat 8 high resolution Sea Surface Temperature using surfers*, Estuarine, Coastal and Shelf Science 265 (2022), p. 107650.
- [18] J. Xie, Z. Lee, X. Li, D. Wang, C. Zhang, Y. Wu, X. Yu, and Z. Zheng, *Estimation of sea surface temperature from Landsat-8 measurements via neural networks*, IEEE Journal of Selected Topics in Applied Earth Observations and Remote Sensing (2024).
- [19] T.R. Loveland and J.R. Irons, *Landsat 8: The plans, the reality, and the legacy*, Remote Sensing of Environment 185 (2016), pp. 1–6.
- [20] J. Jiménez-Muñoz and J. Sobrino, *Error sources on the land surface temperature retrieved from thermal infrared single channel remote sensing data*, International Journal of Remote Sensing 27 (2006), pp. 999–1014.
- [21] J.C. Jimenez-Munoz, J. Cristobal, J.A. Sobrino, G. Sòria, M. Ninyerola, and X. Pons, *Revision of the single-channel algorithm for land surface temperature retrieval from Landsat thermal-infrared data*, IEEE Transactions on Geoscience and Remote Sensing 47 (2008), pp. 339–349.
- [22] X. Yu, X. Guo, and Z. Wu, *Land surface temperature retrieval from Landsat 8 TIRS—Comparison between radiative transfer equation-based method, split window algorithm and single channel method*, Remote Sensing 6 (2014), pp. 9829–9852.

- [23] X. Xiong, A. Wu, B.N. Wenny, S. Madhavan, Z. Wang, Y. Li, N. Chen, W.L. Barnes, and V.V. Salomonson, *Terra and Aqua MODIS thermal emissive bands on-orbit calibration and performance*, IEEE Transactions on Geoscience and Remote Sensing 53 (2015), pp. 5709–5721.
- [24] C. Cao, F.J. De Luccia, X. Xiong, R. Wolfe, and F. Weng, *Early on-orbit performance of the visible infrared imaging radiometer suite onboard the Suomi National Polar-Orbiting Partnership (S-NPP) satellite*, IEEE Transactions on Geoscience and Remote Sensing 52 (2013), pp. 1142–1156.
- [25] B. Luo, P.J. Minnett, M. Szczodrak, K. Kilpatrick, and M. Izaguirre, *Validation of Sentinel-3A SLSTR derived Sea-Surface Skin Temperatures with those of the shipborne M-AERI*, Remote Sensing of Environment 244 (2020), p. 111826.
- [26] J. Tanner, F. Bailleul, S. Bryars, M. Doubell, N. Foster, S. Gaylard, B. Gillanders, S. Goldsworthy, C. Huveneers, C. James, *et al.*, *Potential social, economic and ecological indicators for integrated ecosystem assessment of Spencer Gulf*, Goyder Institute for Water Research Technical Report Series (2019).
- [27] B.D. Bruce, *Preliminary observations on the biology of the white shark, Carcharodon carcharias, in South Australian waters*, Marine and Freshwater Research 43 (1992), pp. 1–11.
- [28] S.E. Wijffels, H. Beggs, C. Griffin, J.F. Middleton, M. Cahill, E. King, E. Jones, M. Feng, J.A. Benthuisen, C.R. Steinberg, *et al.*, *A fine spatial-scale sea surface temperature atlas of the Australian regional seas (SSTAARS): Seasonal variability and trends around Australasia and New Zealand revisited*, Journal of Marine Systems 187 (2018), pp. 156–196.
- [29] Z. Huang, M. Feng, H. Beggs, S. Wijffels, M. Cahill, and C. Griffin, *High-resolution marine heatwave mapping in Australasian waters using Himawari-8 SST and SSTAARS data*, Remote Sensing of Environment 267 (2021), p. 112742.
- [30] Z. Huang, M. Feng, S.J. Dalton, and A.G. Carroll, *Marine heatwaves in the Great Barrier Reef and Coral Sea: their mechanisms and impacts on shallow and mesophotic coral ecosystems*, Science of the Total Environment 908 (2024), p. 168063.
- [31] B. Peña-Molino, B.M. Sloyan, M. Nikurashin, O. Richet, and S.E. Wijffels, *Revisiting the seasonal cycle of the Timor throughflow: Impacts of winds, waves and eddies*, Journal of Geophysical Research: Oceans 127 (2022), p. e2021JC018133.
- [32] M.P. Hemming, M. Roughan, N. Malan, and A. Schaeffer, *Observed multi-decadal trends*

- in subsurface temperature adjacent to the East Australian Current*, *Ocean Science* 19 (2023), pp. 1145–1162.
- [33] G.R. Cresswell and T.J. Golding, *Observations of a south-flowing current in the south-eastern Indian Ocean*, *Deep Sea Research Part A. Oceanographic Research Papers* 27 (1980), pp. 449–466.
- [34] J.A.T. Bye, *Oceanic circulation south of Australia*, *Antarctica Oceanology II: The Australian–New Zealand Sector* 19 (1978), pp. 95–100.
- [35] N.A. Streten, *Southern Hemisphere sea surface temperature variability and apparent associations with Australian rainfall*, *Journal of Geophysical Research: Oceans* 86 (1981), pp. 485–497.
- [36] F. Vivier, D. Iudicone, F. Busdraghi, and Y.H. Park, *Dynamics of sea-surface temperature anomalies in the Southern Ocean diagnosed from a 2D mixed-layer model*, *Climate Dynamics* 34 (2010), pp. 153–184.
- [37] Australian Bureau of Statistics, *Digital boundary files*, <https://www.abs.gov.au/statistics/standards/australian-statistical-geography-standard-asgs-edition-3/jul2021-jun2026/access-and-downloads/digital-boundary-files> (Jul 2021–Jun 2026).
- [38] A. Lewis, S. Oliver, L. Lymburner, B. Evans, L. Wyborn, N. Mueller, G. Raevksi, J. Hooke, R. Woodcock, J. Sixsmith, *et al.*, *The Australian geoscience data cube—foundations and lessons learned*, *Remote Sensing of Environment* 202 (2017), pp. 276–292.
- [39] B. Killough, *Overview of the open data cube initiative*, in *IGARSS 2018-2018 IEEE International Geoscience and Remote Sensing Symposium*. IEEE, 2018, pp. 8629–8632.
- [40] A. Inness, M. Ades, A. Agustí-Panareda, J. Barré, A. Benedictow, A.M. Blechschmidt, J.J. Dominguez, R. Engelen, H. Eskes, J. Flemming, *et al.*, *The CAMS reanalysis of atmospheric composition*, *Atmospheric Chemistry and Physics* 19 (2019), pp. 3515–3556.
- [41] National Oceanic and Atmospheric Administration, National Aeronautics and Space Administration, and United States Air Force, *US Standard Atmosphere, 1976*, National Oceanic and Atmospheric Administration, 1976.
- [42] ECMWF, *IFS Documentation CY43R3 - Part III: Dynamics and numerical procedures*, ECMWF (2017), Available at <https://www.ecmwf.int/node/17735>.
- [43] F. Murray, *On the computation of saturation vapor pressure*, *Journal of Applied Meteorology and Climatology* 6 (1967), pp. 203–204.
- [44] J. Shaman and M. Kohn, *Absolute humidity modulates influenza survival, transmission,*

- and seasonality*, Proceedings of the National Academy of Sciences 106 (2009), pp. 3243–3248.
- [45] Office of Environment and Heritage (OEH), New South Wales Government, *Manly Hydraulics Laboratory waverider buoys - sea surface temperature data*, <https://catalogue-imos.aodn.org.au/geonetwork/srv/eng/catalog.search#/metadata/81c5f192-d4af-4dfe-a660-af15ae46a22a> (2025). Accessed: 2025-02-25.
- [46] C. Emde, R. Buras-Schnell, A. Kylling, B. Mayer, J. Gasteiger, U. Hamann, J. Kylling, B. Richter, C. Pause, T. Dowling, *et al.*, *The libRadtran software package for radiative transfer calculations (version 2.0.1)*, Geoscientific Model Development 9 (2016), pp. 1647–1672.
- [47] ECMWF, *IFS Documentation CY40R1 - Part III: Dynamics and Numerical Procedures*, 3, ECMWF (2014), Available at <https://www.ecmwf.int/node/9203>, operational implementation 22 November 2013.
- [48] USGS, *Landsat 8 Data Users Handbook*, https://d9-wret.s3.us-west-2.amazonaws.com/assets/palladium/production/s3fs-public/atoms/files/LSDS-1574_L8_Data_Users_Handbook-v5.0.pdf (2019).
- [49] T.M. DeCarlo, A.L. Cohen, G.T. Wong, K.A. Davis, P. Lohmann, and K. Soong, *Mass coral mortality under local amplification of 2°C ocean warming*, Scientific Reports 7 (2017), p. 44586.
- [50] K. Unnithan, N. Cherukuru, T. Ingleton, E. Lehmann, M. Paget, Y. Guo, N. Drayson, and G. Kerrisk, *Mapping total suspended solids (TSS) and dissolved organic carbon (DOC) in complex coastal waters using deep learning enhanced remote sensing*, Available at SSRN 5123379 (2025).
- [51] K.T. Peterson, V. Sagan, and J.J. Sloan, *Deep learning-based water quality estimation and anomaly detection using Landsat-8/Sentinel-2 virtual constellation and cloud computing*, GIScience & Remote Sensing 57 (2020), pp. 510–525.
- [52] P.L. Jokiel and E.K. Brown, *Global warming, regional trends and inshore environmental conditions influence coral bleaching in Hawaii*, Global Change Biology 10 (2004), pp. 1627–1641.
- [53] J.A. Sanchez-Cabeza, C.A. Herrera-Becerril, J.L. Carballo, B. Yáñez, L.F. Álvarez-Sánchez, J.G. Cardoso-Mohedano, and A.C. Ruiz-Fernández, *Rapid surface water warming and impact of the recent (2013–2016) temperature anomaly in shallow coastal waters at the eastern entrance of the Gulf of California*, Progress in Oceanography 202 (2022),

p. 102746.

- [54] Y.J. Lee and K. Lwiza, *Interannual variability of temperature and salinity in shallow water: Long Island Sound, New York*, Journal of Geophysical Research: Oceans 110 (2005).
- [55] J. McLean, *et al.*, *Late twentieth-century warming and variations in cloud cover*, Atmospheric and Climate Sciences 4 (2014), p. 727.
- [56] M. Montanaro, J. McCorkel, J. Tveekrem, J. Stauder, E. Mentzell, A. Lunsford, J. Hair, and D. Reuter, *Landsat 9 thermal infrared sensor 2 (TIRS-2) stray light mitigation and assessment*, IEEE Transactions on Geoscience and Remote Sensing 60 (2022), pp. 1–8.
- [57] Y. Guo, K. Mokany, S.R. Levick, J. Yang, and P. Moghadam, *Spatioformer: A geo-encoded transformer for large-scale plant species richness prediction*, IEEE Transactions on Geoscience and Remote Sensing 63 (2025), pp. 1–16.
- [58] N. Pahlevan, B. Smith, J. Schalles, C. Binding, Z. Cao, R. Ma, K. Alikas, K. Kangro, D. Gurlin, N. Hà, *et al.*, *Seamless retrievals of chlorophyll-a from Sentinel-2 (MSI) and Sentinel-3 (OLCI) in inland and coastal waters: A machine-learning approach*, Remote Sensing of Environment 240 (2020), p. 111604.
- [59] Y. Guo, X. Jia, and D. Paull, *Effective sequential classifier training for SVM-based multitemporal remote sensing image classification*, IEEE Transactions on Image Processing 27 (2018), pp. 3036–3048.
- [60] E.T. Gorman, D.A. Kubalak, D. Patel, D.B. Mott, G. Meister, P.J. Werdell, *et al.*, *The NASA Plankton, Aerosol, Cloud, ocean Ecosystem (PACE) mission: an emerging era of global, hyperspectral Earth system remote sensing*, in *Sensors, Systems, and Next-Generation Satellites XXIII*, Vol. 11151. SPIE, 2019, pp. 78–84.
- [61] M. Rice, K. Lapo, K. Hoza, E. Cloutis, M. Kraft, S. Mulcahy, D. Applin, and S. Theuer, *TANAGER: Design and validation of an automated spectrogoniometer for bidirectional reflectance studies of natural rock surfaces*, Earth and Space Science 11 (2024), p. e2024EA003686.
- [62] S. Chabrillat, S. Foerster, K. Segl, A. Beamish, M. Brell, S. Asadzadeh, R. Milewski, K.J. Ward, A. Brosinsky, K. Koch, *et al.*, *The EnMAP spaceborne imaging spectroscopy mission: Initial scientific results two years after launch*, Remote Sensing of Environment 315 (2024), p. 114379.
- [63] D. Krutz, R. Müller, U. Knodt, B. Günther, I. Walter, I. Sebastian, T. Säuberlich, R. Reulke, E. Carmona, A. Eckardt, *et al.*, *The instrument design of the DLR earth sensing imaging spectrometer (DESI)*, Sensors 19 (2019), p. 1622.

- [64] Y. Guo, K. Mokany, C. Ong, P. Moghadam, S. Ferrier, and S.R. Levick, *Plant species richness prediction from DESIS hyperspectral data: A comparison study on feature extraction procedures and regression models*, ISPRS Journal of Photogrammetry and Remote Sensing 196 (2023), pp. 120–133.
- [65] Y.J. Kim, D. Han, E. Jang, J. Im, and T. Sung, *Remote sensing of sea surface salinity: challenges and research directions*, GIScience & Remote Sensing 60 (2023), p. 2166377.